UNIVERSITÀ DEGLI STUDI DI PADOVA

Dipartimento di Fisica e Astronomia “Galileo Galilei”

Corso di Laurea Magistrale in Fisica

Tesi di Laurea

XAFS investigations of bimetallic Ce/Zr-UiO-type metal-organic frameworks

Relatore

Prof. Andrea Sanson

Correlatore

Dr. Kirill A. Lomachenko

Laureando

Alessandro Venier

Anno Accademico 2018/2019

Table of contents

Introduction

Among the recent discoveries in materials a special place is for the Metal Organic Frameworks (MOF), which are micro-porous organometallic compounds usually exhibiting a high degree of crystallization. A brief overview of MOFs is given in chapter 1. Their numerous physical and chemical properties are of interest for industrial applications and fundamental research, especially their high porosity and the ease with which they can be synthetized and modified. However, one of the major problems encountered are their structural resistance to pressure, temperature and chemical reactants, which may be not optimal for these applications. A particular type of MOF which was already known for its extraordinary resistance is the UiO-66 MOF. Originally it contained zirconium atoms organized in octahedra, but recently also cerium atoms have been used, yielding the same type of structure. In this thesis this type of MOF is investigated in its bimetallic form, i.e. when it is synthetized using both zirconium and cerium atoms.

In particular, the property of concern here will be the exact stoichiometric composition of the metallic octahedra, which is not known, nor it is trivially determinable and has an interest due to its relevance for macroscopic properties of the MOFs (e.g. the Ce:Zr concentration ratio dependence of their decomposition temperature (Lammert & al., Tuning the stability of bimetallic Ce(IV)/Zr(IV)-based MOFs with UiO-66 and MOF-808 structures, 2015)).

This question is treated here by use of X-rays, as the scale to be resolved is that of atomic configuration. Also, the EXAFS (Extended X-rays Absorption Fine Structure) spectroscopy seems to be the most appropriate experimental method for this case: selectivity of the atomic specie (by means of choice of the absorption edge) and the local nature of the EXAFS are required to determine the stoichiometry of the metallic octahedra. EXAFS spectroscopy and the theory behind it are described in chapter 2.Thus, absorption spectra of different MOF samples at different Ce:Zr concentration ratios have been acquired at the ESRF synchrotron in Grenoble. The experimental setup employed for the measurement is reported in chapter 3 along with a brief overview of synchrotron radiation.

The analysis of the acquired data is based on hypotheses on the composition of the MOF in types of metallic octahedra, distinguished by their atomic configuration. These

assumptions yield values for the path degeneration parameters appearing in the fitting curve for the EXAFS signals obtained from the acquired spectra. The path degeneration is tightly related to the number of scattering paths for the photoelectrons emitted due to absorption of X-ray photons and the fractions of types of octahedra present in the material at a certain Ce:Zr concentration ratio. It is worth mentioning that the investigated models have the interesting property of requiring only the Ce:Zr ratio to produce the values for the path degeneration parameters, thus reducing in a significative way the number of free parameters for the EXAFS fit. A detailed explanation of the methods of analysis is given in chapter 4, where also the structural models considered for this work are presented.

CHAPTER 1

Metal Organic Frameworks

In this chapter, the physical system under investigation, a metal organic framework, is presented: its physico-chemical properties and its role in applications are illustrated. Starting from the more general context of metal organic frameworks and their characterization and classification, a wide context for this thesis work is given

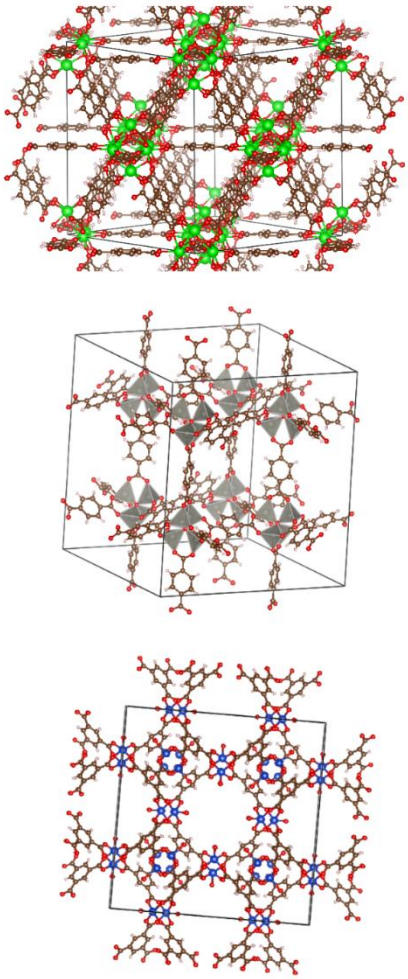

Figure 1.1: Examples of MOFs in their full atomic structure, i.e. from top to bottom: UiO-66, MOF-5 and HKUST-1

1.1 Preliminary considerations

A Metal Organic Framework (abbreviated MOF) is a chemical compound with a well-defined crystalline structure and constituted by two well identifiable types of chemical units: one type that contains metal atoms, also named SBU (Secondary Building Unit) or cornerstones, which are connected one to another by means of the other fundamental part, an organic molecule.

The SBU itself can be just a metals atom or a metal cluster, like a Zn tetrahedron (Li, Eddaoudi, O'Keeffe, & Yaghi, 1999), a Zr octahedron (Cavka & al., 2008), a paddle-wheel-like structure (Chen & al., 2017) and much larger structures (Lin & al., 2012) (Kim & al., 2001).

Also, the linkers could be a number of different organic molecules and it can also be modified after the synthesis process for example by insertion of other organic groups (e.g. amination or oxylation), but the resulting Metal Organic Framework, while chemically

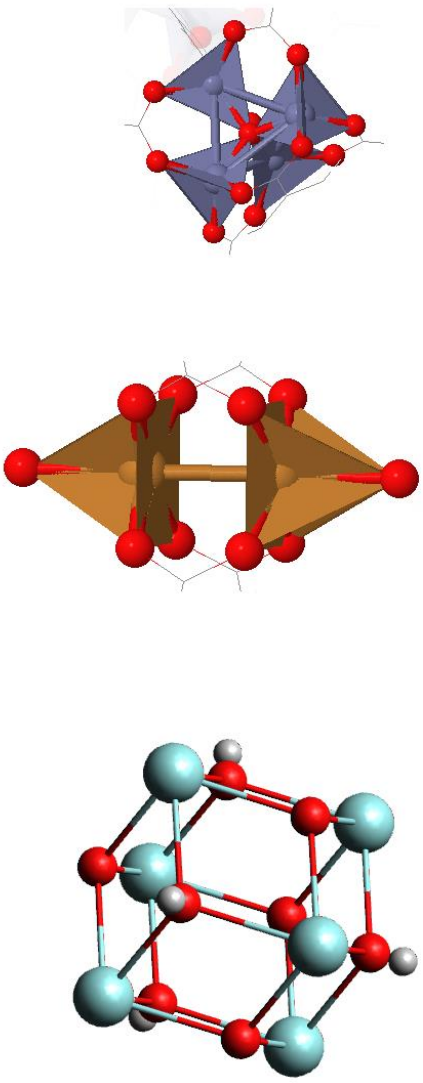

Figure 1.2: Examples of cornerstones in their full atomic form; from top to bottom the MOFs from which they were extracted: MOF-5, HKUST-1, UiO-66

and physically different from the others, may well be related to a well-defined set, as we will see in the following.

It is also usual that the MOF has some voids in its crystalline structure and that the cornerstones are connected to the linkers by coordination bonds. We will see that this is a crucial property that has prompted and followed the research in this field and is very promising for applications. Some illustrative examples of MOFs are shown in Figure 1.1, where it is possible to see some MOFs. As an example, the MOF shown on the top, UiO-66 (after Universitetet i Oslo, where it has been first synthetized), which will be the focus of this thesis, has a metallic octahedral cornerstone, while the middle one (MOF-5 or IRMOF-1) has a Zn tetrahedron as cornerstone. This compound was one of the first MOFs with extraordinary resistance to environments to be described and synthetized (Li, Eddaoudi, O'Keeffe, & Yaghi, 1999).

A MOF is also a Coordination Network, meaning that its structure contains cross links between its chains of repetitive constituents and so it must present a rather complex topology. This is a characteristic rather specific to coordination compounds, due to their great capacity of geometric complexity, almost always given by the presence of chemically versatile metal orbitals, which in this context can be very relevant to synthesis design. In order to highlight the difference between MOF and other (simpler) related structure, like Coordination Polymers (CP) and Coordination Networks (CN), it is worth remembering that in fact MOFs are a subset of CPs and CNs.

These two chemical entities are characterized as repetitive compounds coordinatively bonded, but which need not to be porous and neither have any kind of organic ligands. Also, there is no need to distinguish a cornerstone and a linker, but more simple ligands, which are bridged to give the polymeric structure. Further the MOFs are required to be three-dimensional structures, unlike general CP. It is necessary to notice that the definition given here of a Metal Organic Framework is the one indicated and recommended by the IUPAC, as it can slightly differ from the nomenclature found in the relevant literature (Batten & al., 2012), (Batten & al., 2013).

1.2 Cornerstones

Figure 1.2 presents some examples of cornerstones used in actual synthesis. The presented SBUs are the one for MOF-5, UiO-66 and HKUST-1 (which is acronym for Hong-Kong University of Science and Technology), which are very important examples of MOFs (Lin & al., 2012), (Valenzano & al., 2011). At the top the Zn_4O cornerstone of the MOF-5 is visible: surrounded by the oxygen atoms of the linkers, it has at its center an oxygen atom, but it can be seen geometrically as four interconnected tetrahedra. In the middle there is the Cu_2O_2 cornerstone for HKUST-1, that has a double tetrahedra structure surrounded by the oxygen atoms of the linkers, which in this case are molecules of trimesic acid. It is noticeable that along the proposed line of sight there is evidence of relevant void channels like those appearing in zeolites. The confront between these two (very different) types of materials will be recovered later.

At last, the octahedral-shaped cornerstone of the UiO-66 MOF is chemically composed as $M_6O_4(OH)_4$, where M can refer to tetravalent metals such as zirconium, cerium or hafnium. Each cornerstone is coordinated at the metal atoms (two per each of the ends of the linker) by 12 linkers, which in Figure 1 are BDC (1-4, benzene-dicarboxylate) linkers.

The cornerstones always contain metallic atoms, but almost always also other elements, mostly Oxygen, Carbon and Hydrogen. In the previous examples it has been shown however that the number of atoms in the cornerstones can be very different from one type of MOF to another. The cornerstones are a crucial part for the coordination geometry of the framework and can also be rather useful as the metallic atoms can be active sites for catalysis or adsorption processes. This is related to the fact that these structural units are usually rich

in transition metal atoms, that are well known as active catalysts for different chemical reactions.

Before talking about the linkers, it is necessary to emphasize a point which has been critical for research into this field: the MOFs are in general not so structurally stable as it is required in certain environments (Li, Eddaoudi, O'Keeffe, & Yaghi, 1999). There are also cases of drastic geometrical changes (so called 'breathing transition' in MOF MIL-53 (Bolinois & al., 2017), which do not affect the topology of the network), so it is understandable that in general this class of materials are expected to be far softer than its principal competitors, e.g. Zeolites.

Anyway, one of the breakthroughs that has led to much progress in the field is indeed the discovery of several MOFs with an unprecedented and extraordinary stability and resistance. Amongst the relevant factors to establish the structural stability of the framework is the strength of the ligand-cornerstone coordination bond. Also, a high number of coordination bonds per cornerstone can make a MOF structure more stable, as in the case of the UiO-66 MOF. The metal species used in the cornerstones may also have an important role in determining stability of the framework, due to their different chemistry and physical properties (Lammert & al., 2015).

1.3 Linkers

The organic linkers determine many properties of the MOFs, e.g. structural resistance and porosity. They usually have themselves some symmetric properties, such as a mirror plane or planarity, or a dimension more important than others, which can be then exploited in the structural design of the framework. Some of the linkers used in existing MOFs are shown in Figure 1.3, to illustrate some of the combinatorial possibilities present at synthesis level even with a few cornerstones: as an example, the UiO-66 can be realized synthetically both using Fumaric acid or terephtalic acid. We observe that all of them have a planar structure, some rotational symmetry and mirror planes (at least in their deprotonated form, which is the one present in MOFs). The bottom molecule is the Trimesic acid, which constitutes the paddle-wheel structure present in HKUST-1 and has an evident triangular rotational symmetry.

While crystalline compounds definable as Metal Organic Frameworks are not so recent, since the '80s there has been an exponential growth of their number (Moghadam & al., 2017), (Long & M., 2009). The numbers may slightly vary as the definitions are not so transversal in literature, as was before outlined. This fast evolution is to be attributed probably to the increasingly interesting properties of these materials and is also due to the relative ease with which they can be synthetized from simple raw materials (Reinsch & al., 2016), (Reinsch & al., 2015). The great number of synthetic combinations possible is itself an important factor, given not only by cornerstone and linker variability, but also by other variables, like solvent choice. There is in fact the possibility of changing some final properties of the MOFs using different solvents, as it has been reported for topology, morphology and size change upon using different solvents (Chen & al., 2015), (Hwang & al., 2018). In this context we observe that it is also important to elaborate a way to distinguish and identify MOFs under suitable invariants that may not be the crystallographic groups. We will see later how such a necessity can be practically met.

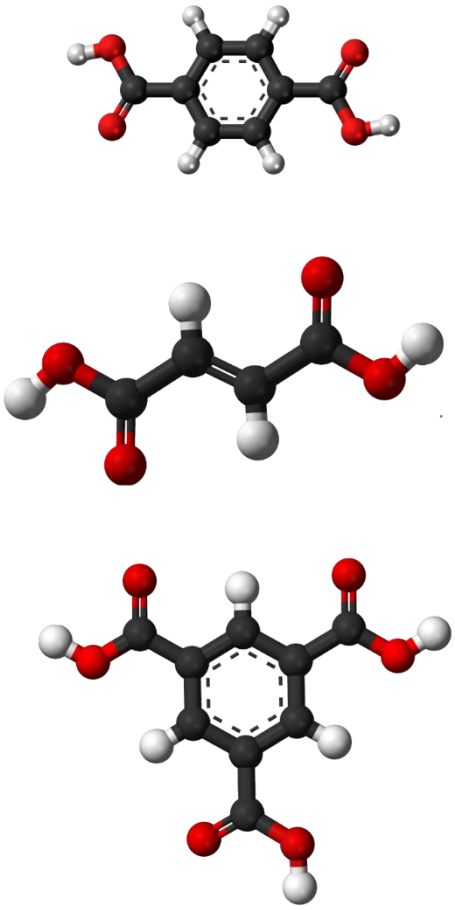

Figure 1.3: Examples of linker molecules which act as ligands in the frameworks; from top: BDC (Terephtalic acid), Fumaric acid, Trimesic acid

It is worth noting that as porous materials the MOFs are the natural successors of the zeolites, a type of mineral well known from centuries for its absorption properties. Zeolites exhibit lower topological freedom, being restricted by having tetrahedral building units and giving their chemical composition, that is not as varied if confronted with the MOFs' one, but generally a greater structural stability, in particular with respect to temperature and typical chemical substances to which catalysts are exposed during reactions (Rhodes, 2007), (Yilmaz, Trukhan, & Muller, 2012).

There are even kinds of coordinative compounds which are known as Zeolitic Imidazolate Frameworks (abbreviated ZIFs)

(Chen & al., 2014) and Zeolitic Metal Organic Frameworks (ZMOFs) (Eddaoudi & al., 2015): they are subsets of MOFs which present several properties in common with zeolites and therefore may be seen as an intermediate compound between them. Another type of materials which is related to MOFs are the Covalent Organic Frameworks, which as their name says are characterized by covalent bonds between light non-metallic elements (Coté & al., 2005). Anyway, they can also be distinguished from a geometrical point of view, since they can be two-dimensional, unlike MOFs.

Considering the high degree of heterogeneity found in this context, it is necessary to introduce classification parameters and criteria, some of which are worth mentioning and describing in detail.

1.4 Topological description and classification

First, there is the topological characterization of the Underlying Net of the reticular material. We have already mentioned the possibility of using topology to describe materials. This is a mathematical object which can be loosely described as the graph which has as nodes the points of connection between linkers and cornerstones, although not exactly at the bonding sites. Other nodes can in fact be cast in to better represent the atomic structure. They are then linked in a way consistent with the overall chemical structure. Some parts of the molecules and of the cornerstones can be formalized as geometrical figures, like triangles and tetrahedrons, to highlight their symmetry (O'Keeffe & Yaghi, 2012). In Figure 1.4 an elementary example illustrates this somehow obscure concept. The presented material is MOF-5, which has the rather simple **pcu-a** (Primitive Cubic Unit in the augmented form) type Underlying Net. It is shown how the various chemical components are reduced and deconstructed into a geometric graph: the cornerstone is abstracted as an octahedron. When the octahedra with vertices on the six carboxylate anions surrounding the cornerstone are collapsed to a point the inherent **pcu** form of the net is retrieved (Li & al., 2014). Given with such a contextual definition it is possible to classify the MOFs under some additional hypotheses regarding their material constituents. We can say this is often done by understanding, classifying and counting the various cycles present in the graph, summarizing symmetrical information into practical mathematical symbols, even if doesn't always give a complete description and discrimination between different topologies.

Topological properties of the underlying net are tightly bound with chemical and physical properties as is understandable from the definition, since it is based mostly on

cornerstones and linkers, which are the basic chemical units. This fact is at the basis of the so called *'reticular chemistry'*, which is fundamental to simplify and plan the synthesis of these complicated materials. As an aside, a basilar fact to be remembered always in this context is that MOFs are periodic and crystalline materials, and this can make topology very complex and complicated.

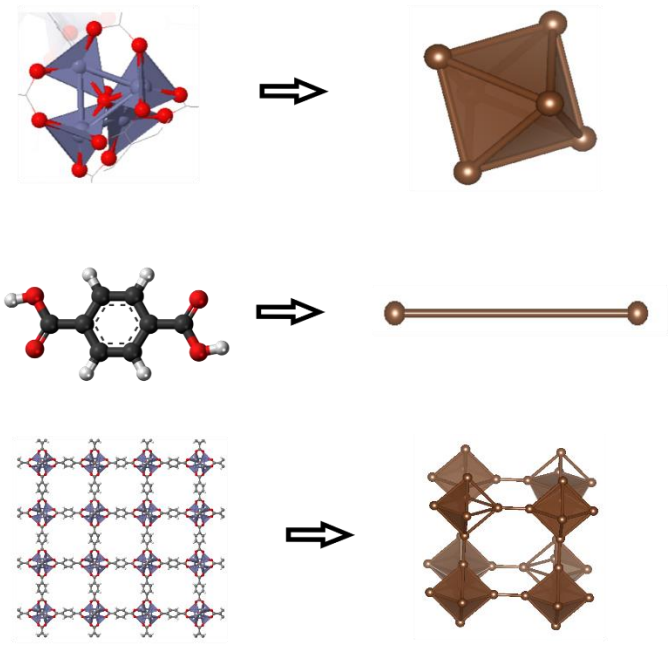

*Figure 1.4: Illustration of the deconstruction process in the elementary case of MOF-5; the cornerstone is six-coordinated with the linkers (BDC) and the resulting net (bottom) is of **pcu-a** type*

As a matter of fact, the topology is useful because it is insensitive to continuous transformations in a precise sense, but in this case the deformations can also be adding of functional/structural groups to the linkers: the underlying net is always the same and so it can direct material design. Further, it has the simple application of simplifying existing databases, which could contain repeated structures just differing by unessential details or could use too much fine or coarse classifications than is required. As an example of this it is sufficient to consider classical crystallographic groups, which can be very susceptible to minor moieties changes at linker level and insensitive to severe changes in overall structure.

A survey study of this topic and further informations about the topological classification can be found in (Delgado-Friedrichs & al., 2007), (Alexandrov & al., 2011), (Blatov & al., 2012), (Ohrstrom, 2015), (Barthel & al., 2018).

1.5 Coordination numbers

An important numeric parameter is the coordination number of the cornerstones with the linkers. It indicates the number of linkers that are connected through coordination bonds to the cornerstones. It is a number that can range from 3 to even 66 with a variety of intermediate possibilities (Bordiga & al., 2010). It is very relevant in determining physico-chemical properties, structural stability and is mostly related to the type of cornerstone used, as in most coordination compounds. Anyway, it is also possible to manipulate the structure by accurate choice of the linker (Lu & al., 2014).

To avoid misunderstanding it is worth saying that in this thesis we will also use the coordination number of the metallic atoms with respect to other metallic atoms in the same cornerstone and we emphasize that they are different parameters, defined in a different context. Further there are many other coordination numbers that can be defined, e.g. among the cornerstone itself. Giving some examples the MOF-5 (Fig. 1.4) can be easily seen as a six-coordinated MOF looking at its topological Net, while inside its cornerstone it is visible that the oxygen atom at the center of the cornerstone itself is tetracoordinated to zinc atoms. For the HKUST-1 instead the cornerstones are tetracoordinated to the trimesate linkers.

It will become clear in the following of the thesis that to establish coordination and in general structure the oxidation state of the metals (which can vary) must be considered.

1.6 Relevant physical and chemical properties

MOFs are a very promising category of materials due to their many interesting properties. It has been already pointed out that much progress in the field has been linked to discovery or breakthroughs in some potentiality that MOFs display. Listing here all these qualities and characteristics would be of no use, if not impossible. Anyway, it is worth highlighting those who deemed to be the most important of them up to now.

Aside from them we can find reported use of MOFs for magnetic materials (Barthelet & al., 2002), for applications in supercapacitors (Hwang & al., 2018) and nanostructures (Malouche & al., 2017), as well as photocatalysis (Pu & al., 2015), sensor probes (Chen & al., 2017), imaging (e.g. magnetic resonance (Peller & al., 2018)) and many other fields.

Many of these can be tuned by post-synthetic modification of their chemical structure and this gives an additional combinatorial factor to the possible preparations.

1.7 Effective surface area and permanent microporosity

The great effective surface area is perhaps the most famous characteristic of MOFs. Some numerical examples can be seen in Table 1.1, with the related extraordinary microporosity (where reported). The presented values are among the highest for microporous materials, even if they can strongly vary with linkers and metal composition. This property is crucial for (heterogeneous) catalysis and more generically for adsorption and absorption. One application in this sense which has attracted attention recently is gas adsorption: it could give concrete applicability to fuel storage, like Hydrogen and Methane. The former is unconventional and thus some microporous-based technology could a fortiori lead to increased availability, while the latter one could be simply made more available and easier to transport in safety (Suh & al., 2012), (Li & al., 2016).

While there are many micro- and meso-porous materials already well known and suitable for these kinds of applications, it is noticeable that the MOFs have a porosity tunable with their chemical composition, e.g. using longer linkers with similar overall structure and given the possibility of stimulated structure changes it may be possible to adapt the technology to the contextual necessities.

Post-synthetic modification is also useful here as the substitution or addition of functional groups or directly other molecules can be used to enhance and/or tune the adsorption effect. It should be noted that also defects can influence adsorption/absorption processes, e.g. as they can enhance diffusion: this quality is important because defects distribution can be engineered and controlled (up to a certain point) like many other properties (Wu & al., 2013).

Another possibility is using MOFs in combination with nanoparticles with a known catalytic role (Malouche & al., 2017). This functionality is facilitated by the fact that nanosized objects can fit well in the framework pores and thus can be controlled in some regards. As a last point, a potentiality resides also in the predictability and stability of the dimensions of the pores: this could be relevant in separation of nanosized objects that cannot fit in the pores. One example in this sense concerns again breathing transitions (Kim & al., 2017).

MOF type	Surface area $[m^2 g^{-1}]$	Porosity volume $[cm^3 g^{-1}]$	Source
Ce-UiO-66-BDC	1282,^	0.50	(Lammert & al., 2015)
Ce-UiO-66-Fum	732,^	0.30	(Lammert & al., 2015)
Zr-UiO-66-Fum	990,^	0.43	(Reinsch & al., 2015)

Table 1.1: Specific values of the effective surface area for some relevant UiO-66 MOF types with Porosity volume values; (^:BET Surface area): this is an estimate of the effective surface area of adsorption; BDC, Fum and TPDC indicate the used linkers.

1.8 Catalysis

The other greater property of MOFs is their catalytic role (at least potential) in many reactions of industrial and scientific interest. While in some cases these materials have better performances than their direct competitors, in other contexts they are outperformed by their porous rivals, i.e. zeolites, clays, alumina, activated carbon and mesoporous silica to cite a few (Yilmaz, Trukhan, & Muller, 2012), (Rouquerol & al., 1994).

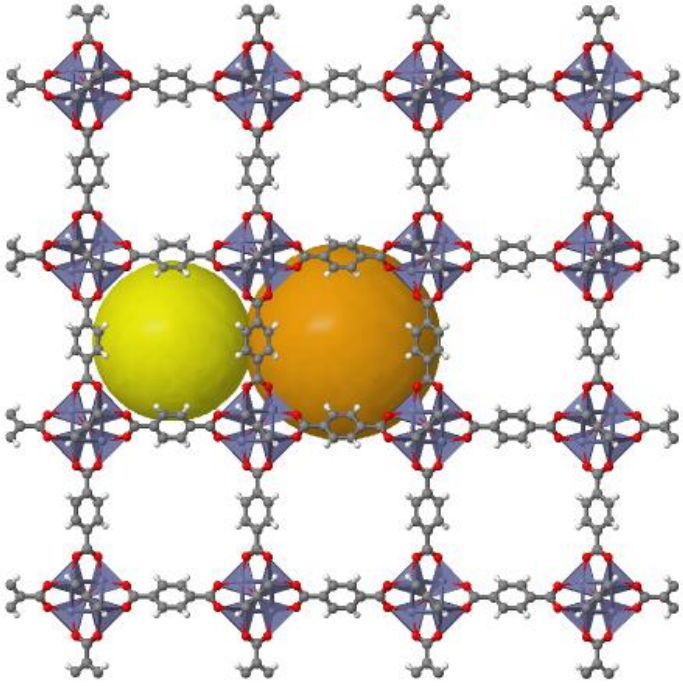

Figure 1.5: Illustration of the microporous cavities of MOF-5; the yellow cavity is delimited by the Hydrogen atoms of the benzyl groups, while the orange one by the faces of the benzyl groups themselves

Anyway, it should be emphasized as before that the interesting applicative potential of MOFs resides mostly in their polymorphism and adaptability. To understand this, it is useful to examine the concept of open site MOF. An open metal site MOF for example exhibits coordinative unsaturation at some metal atoms, thus allowing for interaction between them and host molecules. This can be a crucial property regarding catalytic activity of the material, given the well-known properties of some transition metal species. However even in MOF without open metal site there can still be catalytic opportunities to be taken, as shown in (Smolders & al., 2018), (Lammert & al., 2015).

This concept can be translated to organo-catalysts inside the framework and it is an important factor for catalysis performances as it can be modulated accordingly to synthesis and subsequent modifications. In a MOF there is the possibility of Lewis acidic sites (e.g. on a metal atom), but also basic sites are possible, for example through amination of linkers. As pointed out before, the engineering of defects can be very useful: it can create open sites and enhance diffusion throughout the framework structure, which is important in this context.

As an aside, for most chemical applications it is necessary that the material is "activated", in the sense that it is free from the solvent molecules remained into the pores after the self-assembly of the framework: this is by itself a question of interest, given the multiple practical ways to realize it (Mondloch & al., 2013).

1.9 Experimental methods

To investigate all these properties a series of experimental methodics have been elaborated, some of which we will mention and utilize in this thesis. It is interesting to present them briefly. One simple, but fundamental analysis method is the ThermoGravimetric Analysis (TGA), which consists in monitoring the weight of the compound (that can also be still containing solvent molecules from the synthesis) with the temperature changing. This technique can be useful to investigate the thermal stability of the material and to determine potential defects in its structure (Valenzano & al., 2011). It has already been emphasized the fact that metal organic frameworks have good crystallization properties (at the micrometric scale): these can be exploited to yield X-ray diffraction patterns useful to structure determination, for example using X-Ray Powder Diffraction (XRPD) (Valenzano & al., 2011), (Gàndara & Bennett, 2014), (Tranchemontagne & al., 2008). Given the presence of both organic ligands and metal ions

there is the possibility of investigating the UV-vis range of electromagnetic spectrum, finding properties as the band gap energy separation. In this context of chemical composition, it is also of special interest the Infrared (IR) spectroscopy, which has been useful in determining structural details of cornerstones and obviously can give informations regarding the state of the organic ligands (Valenzano & al., 2011). However, the principal experimental method employed in this work will be the X-ray Absorption Spectroscopy (XAS), particularly in the EXAFS region.

Through this set of techniques, it is possible to investigate physical properties of a material that are local with respect to an atom in an element-selective way, permitting an independent simple way to obtain structural informations (Bordiga & al., 2013), (Bordiga & al., 2010), (Lomachenko & al., 2018), (Lin & al., 2012), (Butova & al., 2016).

1.10 Theoretical investigation

Other than the experimental methods it is also worth mentioning some theoretical ways of inspection which can be employed in studying the MOFs. The simplest (yet still puzzling in some respects) is the already mentioned study of the relations between topology and MOFs properties, but also more sophisticated approaches, such as Ab initio calculations, with Density Functionals or Molecular Dynamics, have found application in this field.

Regarding the DFT theoretical framework, it finds suitable application to establish and predict structure and interactions of the material with guest molecules and particles. This is also useful in terms of modifications of the material (Lee & al., 2015), (Valenzano & al., 2011). For the Molecular Dynamics methods instead, the principal application is for absorption/adsorption, but it can also be used in conjunction with DFT to ease description of certain electronic properties, as for example to understand IR-UV-Vis spectroscopy and related phenomena (Biswal & Kusalik, 2017).

1.11 UiO-66 Metal Organic Framework

At this point it may be useful to introduce more in detail the MOF on which this thesis will focus on. In this work we will study in particular a variant case of the MOF UiO-66. Its reticular components are shown in Figure 1.6 and are arranged in a face centered cubic structure in the crystalline form. The construction of the **fcu** (which stands for Face Centered Unit) underlying net from the atomic structure is analogous to the one illustrated before.

The coordination number of the cornerstones is 12: it is relatively high and gives extraordinary resistance in combination with robust linkers. In fact, the first thermal signs of framework collapse come from the decomposition of the linkers, as it is evident for example using MS spectroscopy (Valenzano & al., 2011). Thus, it is understandable that in this sense the stability of the material cannot be substantially enhanced beyond a certain point without changing the linker molecules. While in this analysis the linker was the fumarate ligand, there are other possibilities which have been realized, always using as cornerstone the same metallic octahedron: BDC (Benzen-1,4-DiCarboxylate), BPDC (BiPhenyl-1,4-DiCarboxylate) (UiO-67), TPDC (TriPhenyl-1,4-DiCarboxylate) (UiO-68), which are very similar molecules, obtained geometrically by adding a Benzene functional group in line with the 1,4-carboxylate groups.

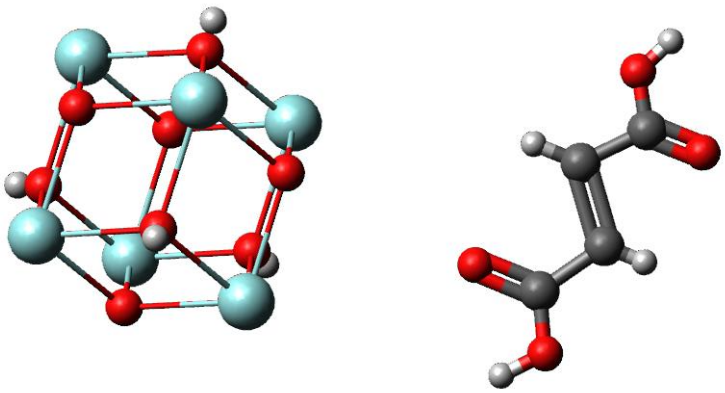

Figure 1.6: Basilar components of the UiO-66(-Fum) MOF type; from left: the $Zr_4O_4(OH)_4$ metallic cornerstone and a molecule of Fumaric acid

Also, there is a deoxylated variant of the cornerstone with different structural and adsorptive properties, as described in (Valenzano & al., 2011). One of the many reasons why this type of MOF is interesting is the possibility of green synthesis of some of its variants with reasonable effort on a scale significant for applications. The structural properties of UiO-66 are remarkable due to its resistance to chemical solvents and strong reactants, high temperature (in its Zr-UiO-66-BDC form it has a collapse temperature of 723 K and a dehydroxylation temperature of 573 K (Vermoortele & al., 2011), which are amongst the highest reported for the variety of MOFs types using this framework structure), relatively high pressure (it is stable at least up to $10000\ Kg\ cm^{-2}$, as evidenced from X-ray Powder Diffraction patterns remaining unaltered (Cavka & al., 2008)). UiO-66 has been

found to contain defects due to missing linkers, which can amount to ~10% of the total linkers (Wu & al., 2013). The quantity of this kind of defects can be tuned and give a greater micro-porosity and adsorption area, although defects can induce a decrease in symmetry (evidenced at space group level for example) and in stability.

All these properties are useful to obtain catalysis related applications and make of the UiO-66 a versatile material. Samples have been synthetized using zirconium, hafnium (Bon & al., 2012) and cerium as the metal for the cornerstones.

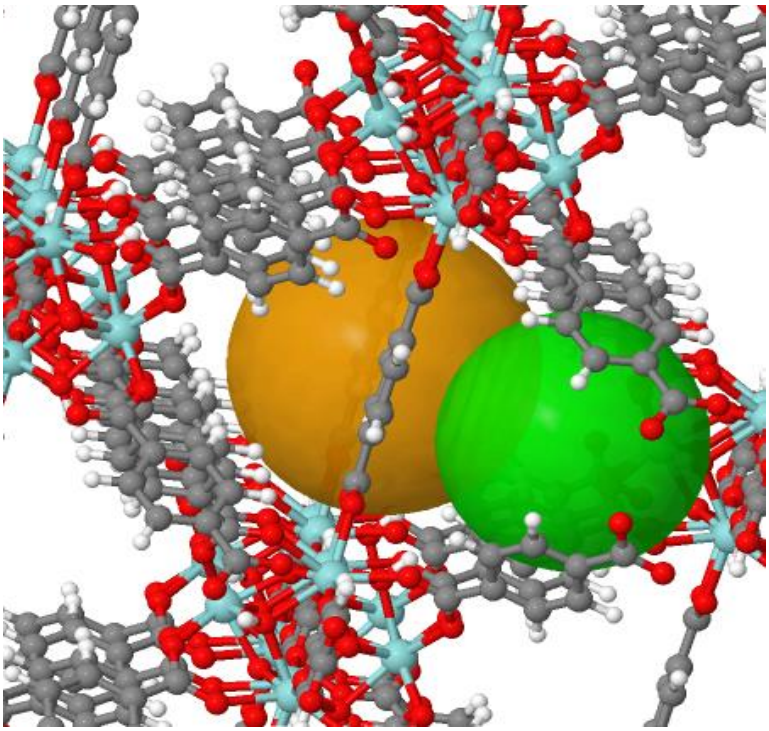

Figure 1.7: Illustration of the microporous cavities of the MOF UiO-66(-BDC)

They are always in the M(+IV) ionic form, at least in the crystalline ideal form but have different physico-chemical properties. In this thesis we will investigate some physical properties of UiO-66 with both Zirconium and Cerium at the same time. One of the goals of the experiments run on the samples synthetized have been determining the metallic stoichiometry of the resulting cornerstones (Lomachenko & al., 2018). The various possibilities of Cerium population of the cornerstones are shown in Figure 1.8. This is a local property and can be investigated by EXAFS spectroscopy, which will be presented in the next chapter. Several interesting properties peculiar to this mixed-metal material have been highlighted in the recent literature: a decreased structural stability with increasing cerium content, quantified for example through decomposition temperature and tunable

structural properties, i.e. crystal lattice parameter, micro-porosity and BET surface area. About this point it is also worth noticing a noticeable change of the decomposition temperature dependence to cerium content at around $[Ce] = 20.6\%$ (Lammert & al., 2015). An important difference with respect to Zirconium based UiO-66 is also the possibility of redox reactions with Cerium, which can pass between the $\mathrm{Ce}(+\mathrm{III})$ and $\mathrm{Ce}(+\mathrm{IV})$ oxidation states.

This can be seen for example in ceria (nominally CeO_2), which is not an exact stoichiometric oxide due to this fact. This chemical property finds its major application in TWC (Three Way Catalytic) converter for vehicles: in this case the Cerium is used as a mean to store Oxygen, so optimizing the stoichiometry of the gaseous mixture to be treated in the converter (Montini & al., 2016). This property has catalytic opportunities, especially in conjunction with other chemical species (Smolders & al., 2018).

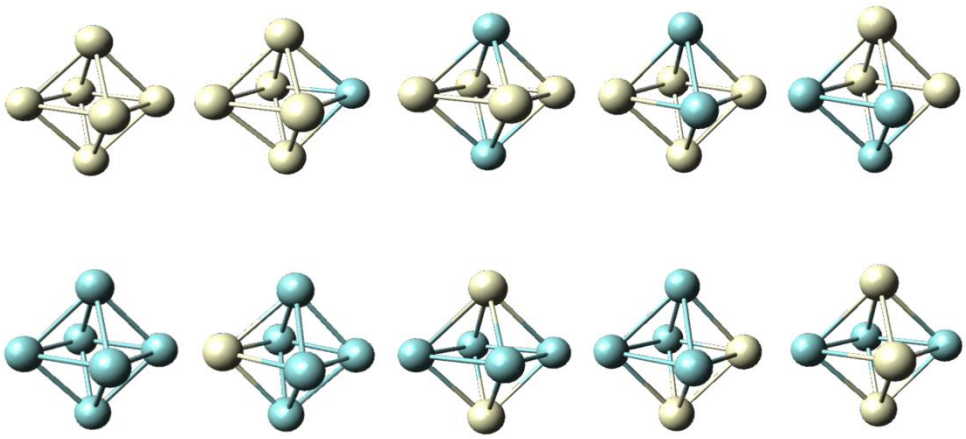

Figure 1.8: Different metallic configuration possibilities for the cornerstone of MOF UiO-66; different colour spheres represent different elements, e.g. Zr and Ce

Bibliography: Chapter 1

Aa., V. (2016). *Macrocyclic and Supramolecular Chemistry: How Izatt-Christensen Award Winners Shaped the Field.* Reed M. Izatt.

Alexandrov, E. V., & al., e. (2011). Underlying nets in three-periodic coordination polymers: topology, taxonomy and prediction from a computer-aided analysis of the Cambridge Structural Database. *CrystEngComm, 13*, 3947.

Barthel, S., & al., e. (2018). Distinguishing Metal−Organic Frameworks. *Cryst. Growth Des., 18*, 1738-1747.

Barthelet, K., & al., e. (2002). [VIII(H2O)]3O(O2CC6H4CO2)3·(Cl, 9H2O) (MIL-59): a rare example of vanadocarboxylate with a magnetically frustrated three-dimensional hybrid framework. *Chem. Commun.*, 1492-1493.

Batten, S., & al., e. (2012). Coordination polymers, metal–organic frameworks and the need for terminology guidelines. *CrystEngComm, 14*, 3001.

Batten, S., & al., e. (2013). Terminology of metal–organic frameworks and coordination polymers (IUPAC Recommendations 2013). *Pure Appl. Chem., Vol. 85, No. 8*, 1715-1724.

Biswal, D., & Kusalik, P. G. (2017). Molecular simulations of self-assembly processes in metal-organic frameworks: Model dependence. *J. Chem. Phys. 147*.

Blatov, V., & al., e. (2012). Vertex-, face-, point-, Schl€ afli-, and Delaney-symbols in nets, polyhedra and tilings: recommended terminology. *CrystEngComm, 12*, 44-48.

Bolinois, L., & al., e. (2017). Breathing-induced new phase transition in an MIL-53(Al)–NH 2 metal–organic framework under high methane pressures. *Chem. Commun., 53*, 8118.

Bon, V., & al., e. (2012). Zr(IV) and Hf(IV) based metal–organic frameworks with reo-topology. *Chem. Commun., 48*, 8407-8409.

Bordiga, S., & al., e. (2010). X-ray absorption spectroscopies: useful tools to understand metallorganic frameworks structure and reactivity. *Chemical Society Reviews, 39*, 4885-4927.

Bordiga, S., & al., e. (2013). Reactivity of Surface Species in Heterogeneous Catalysts Probed by In Situ X-ray Absorption Techniques. *Chem. Rev., 113*, 1736-1850.

Butova, V. V., & al., e. (2016). Metal-organic frameworks: structure, properties, methods of synthesis and characterization. *Russian Chemical Reviews, 85*, 298-301.

Butova, V. V., & al., e. (2019). Partial and Complete Substitution of the 1,4-Benzenedicarboxylate Linker in UiO-66 with 1,4-Naphthalenedicarboxylate: Synthesis, Characterization, and H 2 -Adsorption Properties. *Inorg. Chem.*

Cavka, J. H., & al., e. (2008). A New Zirconium Inorganic Building Brick Forming Metal Organic Frameworks with Exceptional Stability. *J. AM. CHEM. SOC., 130*, 13850-13851.

Chen, B., & al., e. (2014). Zeolitic imidazolate framework materials: recent progress in synthesis and applications. *J. Mater. Chem. A, 2*, 16811.

Chen, D., & al., e. (2015). Solvent-Induced Topological Diversity of Two Zn(II) Metal−Organic Frameworks and High Sensitivity in Recyclable Detection of Nitrobenzene. *Cryst. Growth Des., 15*, 3999-4004.

Chen, Y., & al., e. (2017). A Copper(II)-Paddlewheel Metal−Organic Framework with Exceptional Hydrolytic Stability and Selective Adsorption and Detection Ability of Aniline in Water. *ACS Appl. Mater. Interfaces, 9*, 27027-27035.

Coté, A. P., & al., e. (2005). Porous, Crystalline, Covalent Organic Frameworks. *Science, 310*, 1166-1170.

De Vos, A., & al., e. (2017). Missing Linkers: An Alternative Pathway to UiO-66 Electronic Structure Engineering. *Chem. Mater., 29*, 3006-3019.

Delgado-Friedrichs, O., & al., e. (2007). Taxonomy of periodic nets and the design of materials. *Phys. Chem. Chem. Phys., 9*, 1035-1043.

Eddaoudi, M., & al., e. (2015). Zeolite-like metal–organic frameworks (ZMOFs): design, synthesis, and properties. *Chem. Soc. Rev., 44*, 228-249.

Gàndara, F., & Bennett, T. D. (2014). Crystallography of metal–organic frameworks. *IUCrJ, 1*, 563-570.

Hwang, J., & al., e. (2018). Solvent mediated morphology control of zinc MOFs as carbon templates for application in supercapacitors. *J. Mater. Chem. A, 6*, 23521.

Kandiah, M., & al., e. (2010). Post-synthetic modification of the metal–organic framework compound UiO.66. *Journal of Materials Chemistry, 20*, 9848-9851.

Katz, M. J., & al., e. (2013). A facile synthesis of UiO-66, UiO-67 and their derivatives. *Chem. Commun., 49*, 9449.

Kim, J. Y., & al., e. (2017). Selective Hydrogen Isotope Separation via Breathing Transition in MIL-53(Al). *J. Am. Chem. Soc., 139*, 17743-17746.

Kim, J., & al., e. (2001). Assembly of Metal-Organic Frameworks from Large Organic and Inorganic Secondary Building Units: New Examples and Simplifying Principles for Complex Structures. *J. Am. Chem. Soc., 123*, 8239-8247.

Lammert, M., & al., e. (2015). Cerium-based metal organic frameworks with UiO-66 architecture: synthesis, properties and redox catalytic activity. *Chem. Commun., 51*, 12578.

Lammert, M., & al., e. (2015). Tuning the stability of bimetallic Ce(IV)/Zr(IV)-based MOFs with UiO-66 and MOF-808 structures. *Dalton Trans., 46*, 2425.

Lee, K., & al., e. (2015). Small-Molecule Adsorption in Open-Site Metal−Organic Frameworks: A Systematic Density Functional Theory Study for Rational Design. *Chem. Mater., 27*, 668-678.

Li, B., & al., e. (2016). Porous Metal-Organic Frameworks: Promising Materials for Methane Storage. *Chem 1*, 557-580.

Li, H., Eddaoudi, M., O'Keeffe, M., & Yaghi, O. M. (1999). Design and synthesis of an exceptionally stable and highly porous metal-organic framework. *Nature, Vol. 402*, 276-279.

Li, M., & al., e. (2014). Topological Analysis of Metal−Organic Frameworks with Polytopic Linkers and/or Multiple Building Units and the Minimal Transitivity Principle. *Chem. Rev., 114*, 1343-1370.

Lin, K.-S., & al., e. (2012). Synthesis and characterization of porous HKUST-1 metal organic frameworks for hydrogen storage. *International Journal of Hydrogen Energy, 37*, 13865-13871.

Liu, J., & al., e. (2012). Progress in adsorption-based CO 2 capture by metal–organic frameworks. *Chem. Soc. Rev., 41*, 2308-2322.

Lomachenko, K., & al., e. (2018). Exact stoichiometry of CeZr cornerstones in mixed-metal UiO-66 MOFs revealed by EXAFS spectroscopy. *J. Am. Chem. Soc.*

Long, J. R., & M., Y. O. (2009). The pervasive chemistry of metal–organic frameworks. *Chem. Soc. Rev., 38*, 1213-1214.

Lu, W., & al., e. (2014). Tuning the structure and function of metal–organic frameworks via linker design. *Chem. Soc. Rev., 43*, 5561.

Malouche, A., & al., e. (2017). Hydrogen absorption in 1 nm Pd clusters confined in MIL-101(Cr). *J. Mater. Chem. A, 5*, 23043.

Moghadam, P. Z., & al., e. (2017). Development of a Cambridge Structural Database Subset: A Collection of Metal−Organic Frameworks for Past, Present, and Future. *Chem. Mater., 29*, 2618-2625.

Mondloch, J. E., & al., e. (2013). Activation of metal–organic framework materials. *CrystEngComm, 15*, 9258-9264.

Montini, T., & al., e. (2016). Fundamentals and Catalytic Applications of CeO 2 -Based Materials. *Chem. Rev., 116*, 5987-60414.

Nouar, F., & al., e. (2015). Tuning the properties of the UiO-66 metal organic framework by Ce substitution. *Chem. Commun., 51*, 14458.

Ohrstrom, L. (2015). Let's Talk about MOFs—Topology and Terminology of Metal-Organic Frameworks and Why We Need Them. *Crystals 5*, 154-162.

O'Keeffe, M., & Yaghi, O. (2012). Deconstructing the Crystal Structures of Metal-Organic Frameworks and Related Materials into Their Underlying Nets. *Chem. Rev., 112*, 675-702.

Peller, M., & al., e. (2018). Metal–organic framework nanoparticles for magnetic resonance imaging. *Inorg. Chem. Front., 5*, 1760.

Pu, S., & al., e. (2015). Tuning the optical properties of the zirconium–UiO-66 metal–organic framework for photocatalytic degradation of methyl orange. *Inorganic Chemistry Communications, 52*, 50-52.

Reinsch, H., & al., e. (2015). Green synthesis of zirconium-MOFs. *CrystEngComm, 17*, 4070.

Reinsch, H., & al., e. (2016). A Facile "Green" Route for Scalable Batch Production and Continuous Synthesis of Zirconium MOFs. *Eur. J. Inorg. Chem.*, 4490-4498.

Rhodes, C. (2007). Zeolites: physical aspects and environmental applications. *Annu. Rep. Prog. Chem., Sect. C, 103*, 287-325.

Rouquerol, J., & al., e. (1994). Recommendations for the characterization of porous solids. *Pure & Appl. Chem., Vol. 66, No. 8*, 1739-1758.

Smolders, S., & al., e. (2018). Unravelling the Redox-catalytic Behavior of Ce 4+ + Metal–Organic Frameworks by X-ray Absorption Spectroscopy. *ChemPhysChem, 19*, 373-378.

Suh, M. P., & al., e. (2012). *Chem. Rev., 112*, 782–835.

Tranchemontagne, D., & al., e. (2008). Room temperature synthesis of metal-organic frameworks: MOF-5, MOF-74,. *Tetrahedron 64*, 8553-8557.

Valenzano, L., & al., e. (2011). Disclosing the Complex Structure of UiO-66 Metal Organic Framework: A Synergic Combination of Experiment and Theory. *Chem. Mater., 23*, 1700-1718.

Vermoortele, F., & al., e. (2011). An amino-modified Zr-terephthalate metal–organic framework as an acid–base catalyst for cross-aldol condensation. *Chem. Commun., 47*, 1521-1523.

Waitschat, S., & al., e. (2018). Synthesis of M-UiO-66 (M = Zr, Ce or Hf) employing 2,5-pyridinedicarboxylic acid as a linker: defect chemistry, framework hydrophilisation and sorption properties. *Dalton Trans., 47*, 1062.

Wu, H., & al., e. (2013). Unusual and Highly Tunable Missing-Linker Defects in Zirconium Metal−Organic Framework UiO-66 and Their Important Effects on Gas Adsorption. *J. Am. Chem. Soc., 135*, 10525-10532.

Yilmaz, B., Trukhan, N., & Muller, U. (2012). Industrial Outlook on Zeolites and Metal Organic Frameworks. *Chin. J. Catal., 33*, 3-10.

Zuluaga, S., & al., e. (2016). Chemistry in confined spaces: reactivity of the Zn-MOF-74 channels. *J. Mater. Chem. A, 4*, 13176–13182 .

CHAPTER 2

XAFS spectroscopy

After elucidating the role of Metal Organic Frameworks in the recent scientific research, in this chapter the theoretical background of EXAFS spectroscopy, strongly used for this thesis work, is illustrated. Also, the EXAFS data analysis procedures are outlined from a general point of view, from the procedures employed to derive the EXAFS signal to the fitting curve parametrization and also the evaluation of the fit quality.

2.1 Fundamental physical principles of X-rays

After elucidating the role of Metal Organic Frameworks in the recent scientific research, we will now illustrate the main theoretical background of this thesis. The central mean of investigation used for this work is X-rays, which are produced in a wide variety of physical processes. They can also be classified based on their production method or by more fundamental and objective parameters, physically well defined. As for the production methods, a lot of them have been relevant to the history of science and technology, from the first X-ray tubes at the beginning of the last century to the more sophisticated contemporary synchrotron sources (J. Als-Nielsen, 2001). We will spend more words about X-rays production in the next chapter.

A great number of operative parameters can be defined for such radiations, but first it is necessary to introduce the most fundamental ones: all electromagnetic radiation can be characterized as quanta of the electromagnetic field and these last ones as states identified by the momentum $\vec{p}$ and the helicity. The energy of the electromagnetic field is doubly degenerate upon helicity, which is related to the polarization of the photons by the fact that circularly polarized electromagnetic fields are eigenstates of helicity operator. As for the momentum it is related to the wavevector $\vec{k} = \vec{p}/\hbar$, which in turn defines: the direction of propagation of the quantum of electromagnetic field it is associated to, its spatial periodicity (wavelength) along its propagation direction as a wave through $|\vec{k}| = {}^{2\,\pi}/_{\lambda}$ and its energy

through the Planck relation $E_{\vec{k}} = \hbar c|\vec{k}| = \hbar c\, {}^{2\pi}/_{\lambda}$, where c is the speed of light, ħ is the reduced Planck constant and λ is the wavelength.

This allows to classify electromagnetic radiations by their photon energies. X-rays are usually divided into Soft X-rays, with photon energies between some hundreds of eV and some thousands of eV (KeV henceforth), and Hard X-rays, with photon energies going from the extremal soft X-rays ones to several hundreds of KeV (Attwood) . The precise nomenclature is mostly arbitrary, but it reflects the different processes from which these radiations originate. For example, at upper energies (over 200 KeV) there are Gamma rays, which generally are emitted as a result of nuclear processes. Also, these two major types of X-rays may be very different in their origin and so are their interactions with matter: soft X-rays tend to interact more strongly (i.e. being absorbed more) than hard X-rays. By observing such interactions, many properties of matter can be inspected. Generically speaking, observing a physical feature usually requires a radiation of wavelength at most the same length scale of the detail to be resolved.

Thus, to inspect matter at atomic scale (typically some Ångström) it is expected to use hard X-rays, which have a comparable wavelength (e.g. λ=1.54 Å @8.04 KeV, Cu K_α). There are in fact a lot of experimental methods to inquire physical properties at that level. Before introducing their physical principles, it is necessary to explain what the most important interactions of the X-rays with matter are at these energies.

While at higher energies (above $\sim 250\, KeV$) the dominant interaction mechanism is Compton scattering, the principal one for lower energies is the photoelectric effect, which consists of an electronic transition process involving an (atomic) bound state, either as final or as the initial state (or both). Correspondingly a photon is absorbed or emitted as a consequence of electron transition. If one state is bound, the other can be either another bound state or a continuum state. Emission of a photon by relaxation of excited electrons can follow the absorption event, where the emitted fluorescence photon has lower energy than the absorbed one. Another type of relaxation process is the Auger emission, which results in the emission of a bound electron. There are techniques involving XRD (X-Rays Diffraction), which use the diffraction pattern of X-rays from a crystalline media (or a powder with micro-sized crystallite grain) to assess their lattice parameters and the space group. A very important law of XRD is the Bragg's law, which asserts that the directions of constructive interference pattern are determined after $2\,\vec{k}\cdot\vec{G} = |\vec{G}|^2$, where $\vec{k}$ is the

wavevector and $\vec{G}$ represents a reciprocal lattice vector. This can be translated into saying that the X-ray photon is diffused elastically.

Thus, this technique is usually executed using a single suitable fixed energy monochromatic beam of photons, which must be collimated onto the sample along a certain angle with respect to the sample itself. This is not the case when the physical processes and/or measured signal is of a different kind. For example, in the case of absorption related techniques, the relevant signal, which in case of transmission is absorbance, defined as $A = \log(I_i/I_t)$, where I_i represents the intensity of the beam incident on the sample and I_t represents the intensity of the beam transmitted past the sample. In this case many of the informations available are in the spectroscopic trend, in other words the sampling of the absorbance in function of the photon energy as the independent variable. The definition of the absorbance is given thinking about Lambert-Beer law of absorption, which states that in a homogeneous material the absorbance is directly proportional to the thickness of the path travelled by the incident beam, thus $A = \mu x = \log(I_i/I_t)$, where μ represents the specific absorption coefficient and x the mentioned thickness.

Element name	Atomic number	Mass density [g/cm^3]	l [μm] @1 KeV	l [μm] @10 KeV
Beryllium (Be)	5	1.85	9	$8.37 \cdot 10^3$
Nitrogen (N)	7	$1.25\ 10^{-3}$	$2.4 \cdot 10^3$	$2 \cdot 10^4$
Copper (Cu)	29	8.96	10^{-1}	5.2
Gold (Au)	79	19.30	10^{-1}	4.4

Table 2.1: Attenuation length of some elements, (Keski-Rahkonen & O'Krause, 1974)

The specific absorption coefficient is a property of the material only and is the reciprocal of the absorption length. This last parameter covers many magnitude orders and has a strong dependence from both photon energy and atomic number. Many technological applications of X-rays are based on this physical principle, which for example gives remarkable contrast in medical radiology and in general X-ray imaging.

These dependences are usually summarized in the simple formula (Newville, 2014):

$$\mu \propto \frac{\rho \cdot Z^4}{A \cdot E^3}, \qquad (\mathbf{2.1})$$

where ρ is the mass density of the material, Z the atomic number of the absorbing element, A the atomic mass number of the absorber and E is the incident photon energy. This relationship approximates well the trend of the specific absorption coefficient almost everywhere in photon energy. This is to say everywhere but at some energies, called edge energies. At the edge energies there is a sharp and remarkable increase of μ. Referring to the discussion above, those energies correspond to electronic transitions from deep core states. To refer to those edges in a systematic way the Siegbahn notation is usually employed: the states with n=1,2,3,4 are labelled using the capital K, L, M, N and so the edges corresponding to electronic transition from that state to continuum are also labelled with the same capital letter. Since there are more than one state with principal number n and these in general are not degenerate in energy, a numerical subscript increasing with increasing edge energy can be added (for example L_3 for Ce in this thesis will label the edge for a transition from a $2p_{3/2}$ state).

For suitably high Z it is possible to express an approximate analytical empirical formula for the dependence of the K edge energies upon atomic number Z: $E_{K\_edge} = \alpha \cdot Z^{\beta}$, where $\alpha \approx 5.8\ eV$ and $\beta \approx 2.18$, which is correct up to percent. Regarding the states with energies near to the edge energies it is remarkable that they are often not influenced too much by chemical properties of the physical environment of the atom. For the final states of the photoelectronic transitions instead there is an important dependence from the local atomic surroundings which include the oxidation state of the atom and the structural details of the local environment. In fact, the absorption coefficient may be formally interpreted associating it to a transition event between an initial state $|i>$ and a final one $|f>$ (with density of states in energy $\rho(E_f)$) by means of an interaction described by the H_{int} hamiltonian, that is:

$$\mu \propto \rho(E_f) \cdot |< f|\widehat{H}_{int}|i >|^2 \qquad (\mathbf{2.2}).$$

Thus, it is possible to acquire informations on the final state by measuring the absorption coefficient near the absorption edge. An example of XAS (X-rays Absorption Spectroscopy) spectrum is shown in figure. At this point usually, some definitions are made about the energy ranges: these allow to develop useful theories for all of them. Three regions are defined: the pre-edge, the XANES (X-ray Absorption Near Edge Structure) and the EXAFS (Extended X-ray Absorption Fine Structure) regions (Newville, 2014), as illustrated

in Figure 1. This thesis will focus mainly on EXAFS analysis, so the goal of this section will be of establishing a description of this technique sufficiently detailed for the following data analysis. As for the pre-edge region we will only say that there can be also (pre-edge) peaks (usually found in spectra from transition metals K-edge spectra), that usually correspond to electronic bound-bound transition. Therefore, these can give some information on the state of the absorber and its coordination geometry (Vedrinskii, 1998).

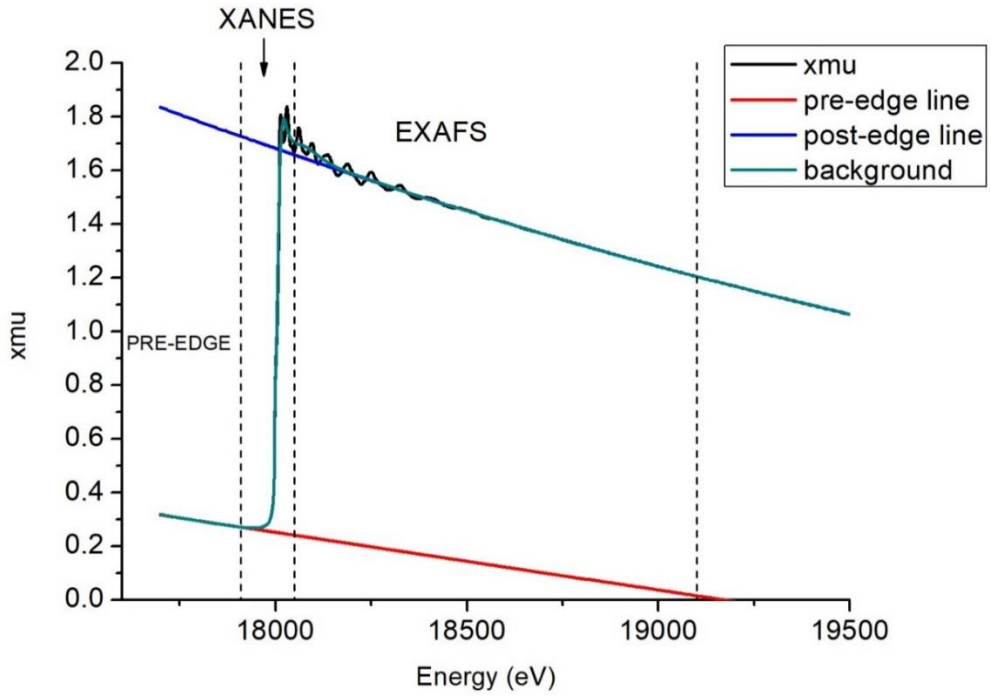

Figure 2.2: Absorption spectrum of a Zr metallic foil, acquired at ESRF

2.2 XANES region

The region following the pre-edge zone is where the rising edge begins to be evident. Here the signal in the energy range up to around 30-50 eV after the edge energy is referred to as XANES (X-ray Absorption Near Edge Structure). Many different transitions contribute to this portion of the spectrum, of both bound-bound and bound-continuum type. The final bound states are energetically near to the continuum and the continuum final states are heavily influenced by scattering of the photoelectron by multiple atoms surrounding the absorber atom. One of the properties that can be investigated by observing this energy regime is the oxidation state of the absorbing atomic specie, which is visible through

features that can be confronted with suitable standards. We will see an example of this in the analysis. XANES region can contain also informations about coordination geometry. A complete theory about this regime is still not established, partly because a full solution of the scattering dynamics is often needed to understand the spectrum (Ravel B. , 1997).

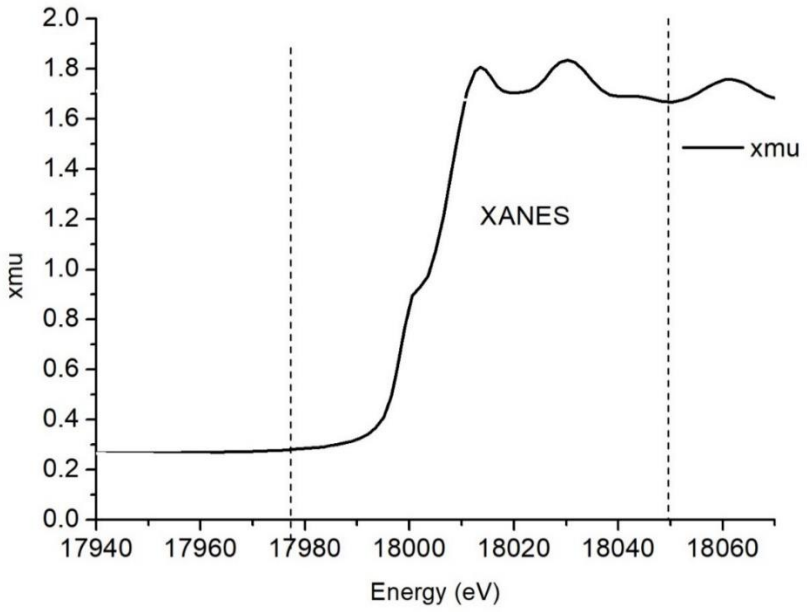

Figure 2.3: XANES region detail for the Zr foil spectrum

2.3 EXAFS semi-empirical theory

The Extended X-ray Absorption Fine Structure as a long history if simple observation is concerned (Lytle, 1999), but its correct theoretical interpretation and exploitation to investigate materials properties is remarkably recent (Sayers, Stern, & Lytle, 1971). In simple terms, it consists of oscillations of the absorption coefficient of a material (in function of the incident photon energy) around a smooth baseline at energies much higher than the edge one.

The fundamental formal idea behind EXAFS spectroscopy analysis is that of investigating the photoelectron final state $|f\rangle$ and consequently the neighbourhood of the absorber (usually up to 5-10 Å) using the informations in the oscillations around the atomic baseline μ_0 of the absorption coefficient. To interpret the spectrum in the post-edge region

a theory can be formulated, which contains some free parameters and leaves a certain freedom on the data analysis. We therefore present a possible approach to this problem: we anyway advise the reader that the following treatment claims to be complete nor rigorous but is only functional to the following data analysis. Before we start with the derivation of the main fitting formula, we must remember that the dynamics of the system is that of a many-body electron system. So, to examine the single particle dynamics, we must somehow (at least formally) split up the final state into an emitted photo-electron single particle state and a core-hole many-body state. However, we will see later how to treat this fact in the fitting model. One possible starting point for the EXAFS theory may be the Fermi Golden Rule, which gives the transition rate $\Gamma_{i\to f} = {2\pi}/{\hbar}\ |\langle f|H_{int}|i\rangle|^2\ \rho(E_f)$, with the final state represented as a continuum state of the independent atom $|f_0\rangle$ plus a perturbation $|df\rangle$ induced by back-scattering from neighbouring atoms that is, in formulas, $|f\rangle = |f_0\rangle + |df\rangle$. At this point a first order approximation in ${\langle df|H_{int}|i\rangle}/{\langle f_0|H_{int}|i\rangle}$ yields the following expression for the absorption coefficient:

$$\Gamma_{i\to f} \propto \Gamma_{i\to f,0} \cdot \left(1 + Re\left[\frac{\langle df|H_{int}|i\rangle}{\langle f_0|H_{int}|i\rangle}\right]\right), \qquad (\mathbf{2.3}).$$

We can then analyse the various parts of this expression. The initial states |i> are deep core level atomic states: these are hardly affected by outer shell electronic configuration and so can be modelled in a relatively easy fashion. As for the H_{int} operator, it can be extracted from the full electrodynamical Hamiltonian, which is the sum of two terms, the electronic term and the free electromagnetic term: $H = H_e + H_{em,free}$. The $H_{em,free}$ term describes the free propagation of electromagnetic fields, while H_e can be expressed using the free electronic Hamiltonian and using the minimal coupling to electromagnetic potential, that is $H_e = {(\vec{p} + e\vec{A})^2}/{2m_e}$, where $\vec{p}$ is the photoelectron momentum. When expanded, this term yields the following terms in Coulomb gauge $\vec{\nabla} \cdot \vec{A} = 0$: $H_{int} = \frac{e}{m_e}\vec{p} \cdot \vec{A}$. A first term which is the free electron Hamiltonian, the second is an interaction term in first order with respect to e and the electromagnetic vector potential $\vec{A}$, in formulas $H_{int} = \frac{e}{m_e}\vec{p} \cdot \vec{A}$ and at last, the third is a term of the second order in e and $\vec{A}$ and we will neglect with respect to the first order one. We can then expand the electromagnetic field in stationary waves and using the dipole approximation, that is neglecting the electromagnetic field spatial dependency in the

imaginary exponential factor $e^{i\vec{k}\cdot\vec{r}}$ (loosely as the zeroth-order term in a series expansion in $\vec{k}\cdot\vec{r}$) yields: $\mu \propto |\langle f|\vec{\epsilon}\cdot\vec{r}|i\rangle|^2$, where $\vec{\epsilon}$ represents the polarization vector of the photon. This expression can be suitably integrated upon directions to give a meaningful experimental observable.

To finish the calculation, we must then say something about the final state $|f\rangle$. Indeed, in the case of this experimental techniques, the interesting physical informations are mostly contained in the final state, as stated in the above, while the initial states and the interaction Hamiltonian are quite universal. This operation is in general very difficult because the involved details of the material required calculations whose extension is not known a priori and gives no well-defined procedure to approach them in general and in a feasible way. Thus, while this approach is correct and essentially intuitive about the physical meaning of every object in play, there is at least another formalism which allows an equivalent theory to be built, affordable calculation to be computed and furnishes us with a rather intuitive and classical way of thinking the photoemission process, i.e. the multiple scattering expansion. This is the formalism of Green's functions, which has also the advantage to compactify the notation. In fact, the Green's functions allow to express the photoelectron final state value at the absorber atom starting from the initial state. Thus, the fundamental scattering problem can be formulated as solution of the so-called Dyson equation, which can be briefly and formally written as: $G = G_0 + G_0 T G_0$, where T is the atomic scattering matrix. This equation can be solved in G as $G = (1 - G_0 t)^{-1} G_0 = \sum_n (G_0 t)^n G_0$, using the single site scattering matrix t. The last step expresses the inverse of the operator $(1 - G_0 t)$ as a Neumann series (also referred to as Born expansion). This is useful as μ can be written using the Green function G as (Ravel B. , Chap. 11: "Quantitative EXAFS Analysis", 2016):

$$\mu \propto \langle i|(\vec{\epsilon}^{*}\cdot\vec{r})\, G(\vec{r},\vec{r}';E)\, (\vec{\epsilon}\cdot\vec{r}')|i\rangle, \qquad (\mathbf{2.4}).$$

A pictorial interpretation of this formalism is given using scattering paths along which the photoelectron undergoes elastic scattering: the $G_0 t G_0$ terms are interpreted as single scattering paths, with the photoelectron propagating freely until it scatters at a neighbour atom, with parameters given by t and then propagates back, while the $G_0 t G_0 t \ldots t G_0$ terms are interpreted as representing multiple scattering paths for the photoelectron.

At this point the crucial property of initial states of being very localized bound states comes into play: we can say that the transition amplitude is (in good approximation) dependent only of the value of the final state at the absorbing atom.

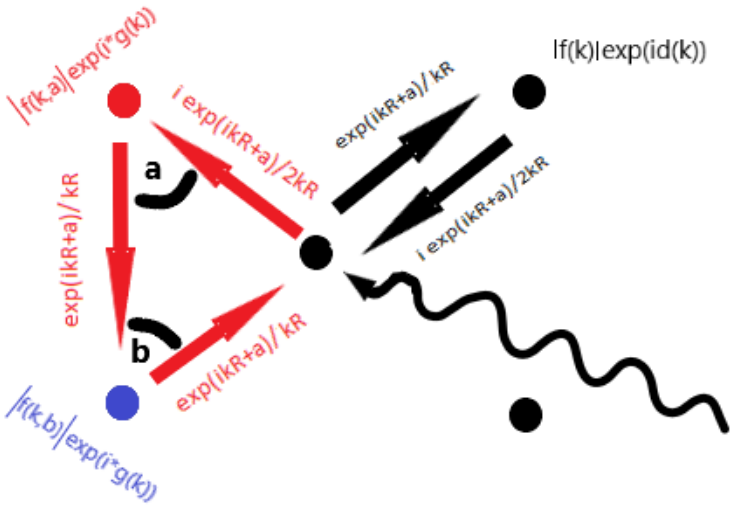

Figure 2.3: Pictorial description of EXAFS theory; the undulated line represents an X-ray photon, while the other arrows represent scattering paths for the emitted photoelectron. Along the paths and at the scattering atoms are reported the various multiplying factors

Thus, it can be proved that this leads to the following form for χ(k), written for a single scattering path:

$$\chi(\mathrm{k}) = |f(k,\pi)| \cdot \frac{\sin\big(2kR + \varphi(k)\big)}{(kR)^2}, \qquad (\mathbf{2.5})$$

where k is the momentum, R represents the distance between the scatterer and the absorber, $f(k,\pi)$ is the backscattering amplitude at momentum k, which is related to energy by the well-known formula $k = \sqrt{\frac{2m_e}{\hbar^2}(E - E_0)}$, $\varphi(k)$ is the phase shift for the backscattering of a photoelectron of momentum k plus the phase shifts due to the paths between the atoms.

The origin of the various factors can be recognized in the previous Born expansion if the SS (Single Scattering) EXAFS equation is written as:

$$\chi(k) = i\frac{e^{ikR}}{2kR}(|f(k,\pi)|)e^{i\varphi(k)}\frac{e^{ikR}}{kR} + c.c., \qquad (\mathbf{2.6})$$

where the first factor represents the free propagator between the absorber and the scatterer, the second, the third and then the real part of the expression is taken. It is important to make clear that up to this point we have made the unrealistic assumption that the atoms composing the material are in a particular position fixed in time. At this point the parameters occurring in the equation can be theoretically calculated, namely the phase shift $\varphi(k)$ and the atomic scattering amplitudes $|f(k,\pi)|$.

There exist some softwares which allow to calculate those parameters self-consistently (Bordiga & al., 2010). One such is FEFF (Rehr, 2010) and we will use it in this thesis work (specifically the Demeter package. The calculations are often performed through a muffin-tin approximation to approach the interatomic potential formalization. It is worth remembering that it assumes that the potential has a certain attractive spherically symmetric form in spherical regions centered on the atoms and outside of them takes a constant value. This raw approximation yields a great simplification in the results and lightens the computational burden.

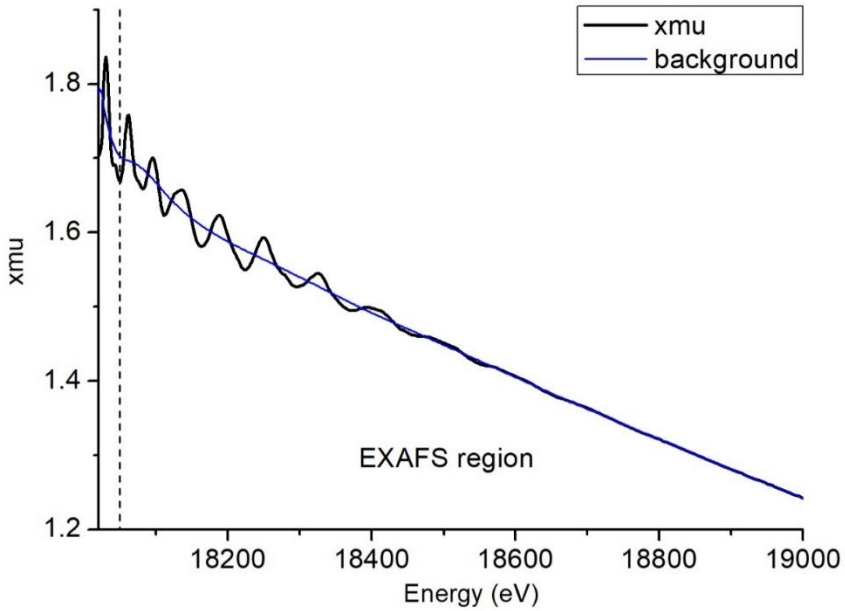

Figure 2.4: EXAFS region detail for the Zr foil spectrum. The EXAFS oscillations are well distinguishable from the background at sight up to 600 eV over the edge energy (nominally 17998 eV)

2.4 Analysis preliminaries and data pre-processing

The experimental working environment can greatly affect the measured signal (i.e. $x\mu(E)$). When samples are prepared, their thickness is usually not known and above all the thickness of the region investigated by the incident beam can be practically impossible to measure. Also, there might be issues with energy stability of the beam, which is not perfectly guaranteed, and even with intensity stability of the beam, which can change over time. For the first problem a solution is imperative to obtain objective and reproducible results: a reference sample is usually employed, as we will see in the next chapter.

The fine structure of the spectrum is yet to be identified and extracted from the total signal. A pre-processing procedure is therefore needed. There is no uniquely defined method to obtain the EXAFS signal and we follow the procedure as is usually performed by the Demeter package (Ravel, (2005)). Pre-processing is usually constituted by at least three steps: calibration, aligning and normalization. The data we will analyse in the last chapter have been treated in this way. Another step usually employed to obtain the signal to be fitted is a forward Fourier Transform from k-space (corresponding to photoelectron momentum) to R-space (corresponding to spatial distances around the absorber atom) We will proceed by exposing them as they have been normally executed for example in this thesis work.

The first step is energy calibration: it is indispensable to correctly relate different datasets, which are often present. In fact, it must be assured that all spectra (at a specific edge) are referencing to the same energy scale. As a matter of fact, it is sufficient that all the spectra are well aligned relatively to one arbitrarily chosen. This is often obtained by choosing one spectrum for which some feature is known as standard, then it is usually enough to shift it until the feature is in the desired place. Aligning follows as all other spectra are shifted to match the calibrated standard with a specific feature. This procedure is often executed upon spectra taken from reference samples, that are well known, using the same experimental setup to take in account possible discontinuities in beam operation, as will be explained in more detail in the next chapter. Attached to the reference sample spectrum is the spectrum of the measured sample. As for calibration the features taken as reference point can be chosen in various alternative ways, the most used is the energy corresponding to the maximum of the derivative of xμ(E). This energy is often labelled as E_0, which is usually given the value of the standard edge energy and can be also be interpreted as the energy of

the corresponding transition (with some caution). We will later see that this is a parameter relevant to EXAFS analysis.

After this part, the normalization procedure follows and defines the EXAFS signal, usually denoted as χ(E). This again can be done in some different ways, which depend on which kind of function is used as the normalization factor and which function of energy is used as the baseline to be subtracted from the whole signal. As for the normalization factor, for example the post-edge interpolation curve can be used. An interpolation background curve that can be interpreted as the atomic (bare) absorption coefficient (usually a third order spline or even higher) is then used as the baseline μ_0 for EXAFS oscillations. In formulas:

$$\chi(\mathrm{E}) = {(\mu - \mu_0)}/{\mu_0} \quad \text{or} \quad \chi(\mathrm{E}) = {(\mu - \mu_0)}/{\Delta_{edge}},$$

where $\Delta_{edge} \equiv \mu_{post-edge}(E_0) - \mu_{pre-edge}(E_0)$.

A possible procedure to remove the background, but at the same time not affect in the subtraction process the physically relevant part of the signal is based on imposing the minimization of the low R (defined as for R lower than some arbitrary cut-off, usually chosen around 1 Å, motivated by the fact that practically all involved atomic radii are greater than this) portion of the forward Fourier transform of the resulting EXAFS χ(k) signal (where $k = \sqrt{\frac{2m_e}{\hbar^2} \cdot (E - E_0)}$), which is interpreted informally as corresponding to broad oscillations due to remaining background components.

2.5 Cumulants expansion and inelastic mean free path

The formalization of the fitting curve is not yet finished at this point: at least two physical facts must be included in the model. The first is the disorder in the material: as we have seen the atomic positions cannot be realistically assumed to be fixed in time and it may present a microscopic structure far from crystalline. Also, we must consider the finite lifetime of the electron core-hole pair.

To account the former aspect, it must be pointed out that the measured EXAFS signal is an average of the above formula over all the possible absorbers (at the same edge) and

scattering paths. We can formalize this way of thinking by introducing a radial distribution function g(R), which is a probability density of the path length R. The measured EXAFS signal can be then viewed as the mean of the χ(k) function above over g(R). This allows a simple interpretation of some feature observed in real data, for example the attenuation or deformation of the peaks, by expanding the average signal in cumulants. This can be done approximating of the EXAFS signal by averaging only the imaginary exponential factor, which is expected to be the contribution most sensible to the environment variability. This average is then expanded as follows:

$$\langle \exp(i \cdot 2kR) \cdot \exp(-{}^{2R}/_{\lambda(k)}) \rangle_{g(R)} = \exp(\sum_{1}^{+\infty} C_n \, {}^{(i2k)^n}/_{n!}), \qquad \textbf{(2.7)}$$

where the C_n are the cumulants. Most of them will not be very relevant to this analysis, as we will truncate the expansion at the second cumulant, but it is worth remembering that the higher order terms (mainly the third and fourth cumulant) are often necessary for data analysis (Newville, 2014), (Dalba, 1999), (Sanson, 2010). During the fit procedure of a peak, the first cumulant may be seen as the position of the centroid of the peak, the second as its average square width around its centroid, the third is related to the skewness of the peak itself and the fourth to its kurtosis.

As for the second problem highlighted in the above, the photoelectron can interact with neighbouring atom scattering elastically or inelastically. The first case is treated in the theory outlined above, while to account for the second type of process it is sufficient to add an exponential factor $\exp(-{}^{2R}/_{\lambda(k)})$ (which accounts for back and forth path of the electron). As for the lambda parameter, it represents the photoelectron mean free path in the material. The main contribution to this parameter comes from the finite core-hole lifetime and the inelastic photoelectron scattering. It can be theoretically estimated and depends on the momentum of the photoelectron. In the typical range of momentum of the photoelectrons involved in EXAFS, the value of the mean free path doesn't exceed significantly 10 Å. So, while also the δk (that is the resolution in k) limits the maximum distance (actually the maximum path length) observable, the mean free path of the photoelectron constraints it more severely and is indeed one of the main physical principles behind the local nature of EXAFS.

2.6 EXAFS data analysis

Having illustrated the fundamental theory of EXAFS, we now pass on to the data analysis procedures. It is worth giving an idea of the typical values of the ranges of k over which the data are acquired: as we have already indicated, the fine structure is visible from around 50 eV above the edge energy up to 2000 eV, which roughly correspond to the k-range [3:23] $Å^{-1}$. A weighting factor of k^w (where w is usually 1, 2 or 3) may be added to highlight the higher k contributions, which are usually hindered by noise and however usually carry some valuable information. Also, the R range over which the fitting procedure is done is very relevant to the analysis, because it heavily restrains the fit quality.

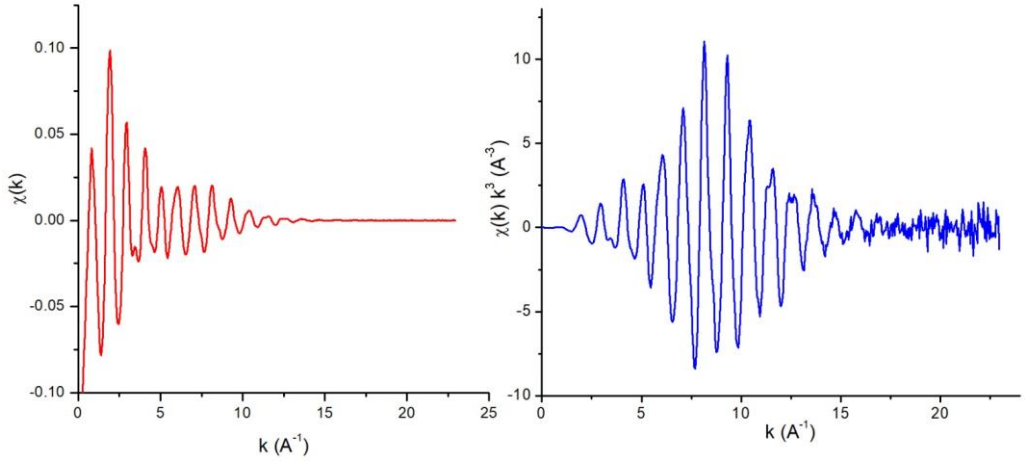

Figure 2.5: The EXAFS signal χ(k) as extracted from the above Zr metallic foil spectrum by background removal (left) and weighted with a k^3 factor (right). The effect of the weight is evident in the higher k range

It makes sense to individuate the various shells contributions to the fine structure, especially when single peaks are identifiable, and fit them separately in a compatible way (e.g. using the same amplitude for all the shells of the same spectrum). A further step is the Fourier transform of the weighted and filtered signal, which may reveal a shell structure of the material, sometimes with the contributions from the different shells of similar distance scatterers around the absorber neatly distinct. After the parametrization of the fitting curve a least square deviations fitting procedure is applied. The number of degrees of freedom can then be estimated roughly as $(\Delta k \cdot \Delta R \frac{2}{\pi})$ and represents the maximum number of free parameters allowable in the fitting model.

2.7 EXAFS fitting curve parametrization

However, some other fitting parameters must be added to this version of the theory: since many of these and the already mentioned parameters will appear recurrently in the following, it is worth briefly illustrating their physical significance and the role they will play in the fitting (Bunker, (2010)), (Calvin, 2013). $S_{0,abs}^2$ is the parameter that is used to introduce the anelastic effect of the processes of photoemission, which involve also the core electrons, i.e. an attenuation of the signal. It is worth noticing that this damping factor is hereupon assumed to be uniform, i.e. S_0^2 is taken as independent of k. This is not at all obvious, nor it is a settled theoretical question.

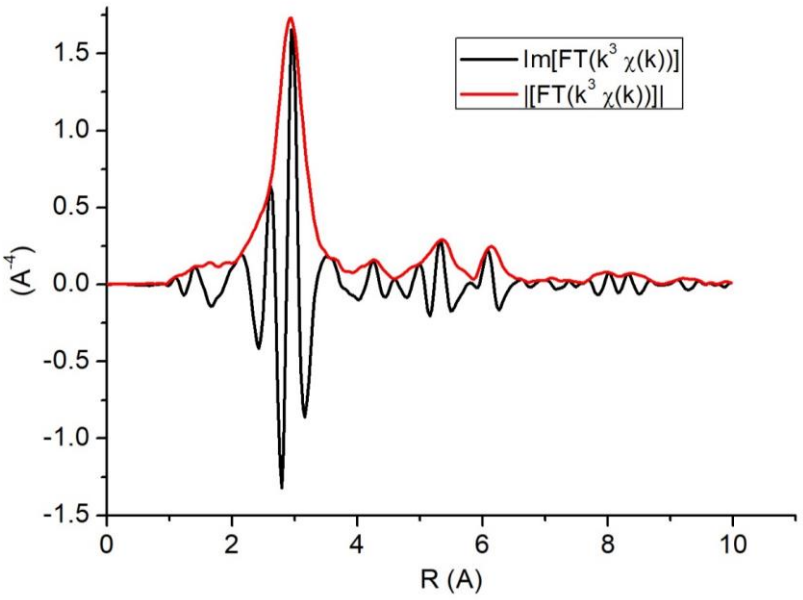

Figure 2.6: Magnitude and imaginary part of the Fourier transform of the EXAFS reported in the previous image. The major peaks are representing the contribution from the corresponding coordination shell of scatterers

A possible physical representation of this factor is $|\langle\psi_{N-1,f}|\psi_{N-1,i}\rangle|^2$ (Fornasini, 2015), where $|\psi_{N-1,i}\rangle$ and $|\psi_{N-1,f}\rangle$ are respectively the initial and final state of the core electrons. In this way it may be observed that this parameter should have a value slightly less than one. Also, we can simplify the fitting model by using the same S_0^2 whenever the absorbing atoms of the same element in different samples have a sufficiently similar electronic core structure.

Since the signal must be averaged over all possible scattering paths, a parameter N_{path} must be introduced in the model to account for the degeneracy due to equivalent scattering paths. This parameter is in fact fundamental to the present analysis and we will dedicate a paragraph to its modelization in the present work at the end of this chapter. It must be highlighted that this parameter is completely correlated with its corresponding S_0^2. Thus, any significative analysis aimed at the determination of this parameter must be able to control this correlation, for example by using more than one dataset with the same S_0^2 parameter. This is how the question has been handled in this analysis. In the following this parameter will also be referred to as coordination number, since in certain cases (e.g. single scattering paths) it corresponds to the number of atoms of the scatterer type in a certain coordination shell for the absorbing atom.

Another important fitting parameter is the ΔE_0, which quantifies corrections to the edge energy indicated at pre-processing level. To understand why this is necessary, we must consider that while edge energies are tabulated for elements (and are well-known for some of their chemical states), uncertainty of beam energy may slightly alter the edge region. Also, the very choice of the edge energy E_0 during the pre-processing has a certain level of arbitrariness, as was illustrated before. For these reasons, a correction (which is typically of some eV) is expected to be introduced.

Passing on to the cumulants, ΔR is the difference between the first cumulant and some a priori distance (usually obtained with crystallographic methods) used to formulate the theorical calculation. It is an important quantifier of local structural deformations and may be used to obtain informations about interatomic correlations (Fornasini, 2001). This is due to the fact that the dynamics of the photoemission process and backscattering is characterized by scales of time much shorter than that of atomic thermal oscillations (core-hole lifetime around $10^{-15}\,s$ versus characteristic time scale of the latter, which can be roughly estimated as ${\omega_{Debye}}^{-1} \sim 10^{-13} s$).

The σ_{path}^2, usually called Debye-Waller factor or second cumulant of the radial distribution function, represents the degree of disorder of the neighbourhood of the absorber atom relatively to a scattering path. Thus, it is in general necessary to introduce a different Debye-Waller factor for every different path. However, in most practical cases this is not due, as the Debye-Waller of the multiple scattering paths can be approximated as the

weighted sum of Debye-Waller of their sub-paths. All this elaboration leads us to write the so-called EXAFS equation, which is usually written as follows:

$$\chi(k) = \sum_{path} (N_{path} \cdot S_{0,abs}^2 \cdot e^{-2R_{path}/\lambda(k)} e^{-k^2 2\sigma_{path}^2} \cdot sin\left(2kR_{path} + \delta(k)\right) \cdot \prod_j \frac{|f_{scatt,j}(k,\gamma)|}{R_j}),$$

with γ as the scattering angle and R_j the path length between the (j-1)-th scatterer and the j-th one. This cumbersome formula significantly reduces to the following in the case of single scattering paths only:

$$\chi(k) = \sum_{SS\ path} (N_{path} \cdot S_{0,abs}^2 \cdot e^{-2R/\lambda(k)} e^{-k^2 2\sigma_{path}^2} \cdot sin\left(2kR_{path} + \delta(k)\right) \cdot \frac{|f_{scatt,path}(k,\pi)|}{(R_{path})^2}).$$

As a final remark, it is very useful to highlight the procedure for the assignation of significant uncertainties to the fitting parameters and for the statistical evaluation of the fitting results. While the first aspect may in principle become very involved, requiring the full consideration of experimental, theoretical and computational details, the question may be settled down by acquiring the same spectra more than one time and analysing them separately. Once the best fit parameter of the various sampled spectra is obtained, for example, the root mean square of them all can be interpreted as the uncertainty of their mean.

As for the statistical significance of the fitting procedures, we will use the reduced chi-square $\chi_v^2 = \chi^2 / (N_{ind} - N_{par})$ and the R-factor, defined as $R = \frac{\sum_i |y_{data,i} - y_{fit,i}|^2}{|y_{data,i}|^2}$ to evaluate the quality of the fit results.

The local nature of EXAFS investigation is one of its characteristic features and is crucial for the analysis in this work. In fact, the property we will investigate in the following, which is the metallic stoichiometry of a MOF cornerstone, is a local one whose precise determination is unfeasible through experimental techniques involving primarily the long-range order of the material, for example XRD (X-Ray Diffraction). This is one of the main reasons why XAFS has been chosen, at cost of the more sophisticated experimental setup, that will be described in the next chapter.

Bibliography: Chapter 2

Attwood, D. (s.d.). *Soft X-rays and extreme ultraviolet radiation.* Cambridge University Press.

Bordiga, S., & al., e. (2010). X-ray absorption spectroscopies: useful tools to understand metallorganic frameworks structure and reactivity. *Chemical Society Reviews, 39*, 4885-4927.

Bunker, G. ((2010)). *Introduction to XAFS_ A Practical Guide to X-ray Absorption Fine Structure Spectroscopy.* Cambridge University Press .

Calvin, S. (2013). *XAFS for everyone.* CRC Press Taylor & Francis Group.

Dalba, G. e. (1999). Sensitivity of Extended X-Ray-Absorption Fine Structure to Thermal Expansion. *Phys. Rev. Lett., Vol. 82, 21,* 4240-4243.

Fornasini, P. (2001). Study of lattice dynamics via extended x-ray absorption fine structure. *J. Phys.: Condens. Matter 13*, 7859-7872.

J. Als-Nielsen, D. M. (2001). *Elements of Modern X-ray Physics.* John Wiley & Sons.

Lomachenko, K., & al., e. (2018). Exact stoichiometry of CeZr cornerstones in mixed-metal UiO-66 MOFs revealed by EXAFS spectroscopy. *J. Am. Chem. Soc.*

Lytle, F. W. (1999). The EXAFS family tree: a personal history of the development of extended X-ray absorption fine structure. *J. Synchrotron Rad. 6*, 123-124.

Newville, M. (2014). Fundamentals of XAFS. *Reviews in Mineralogy and Geochemistry, Vol. 78,* 33-74.

Ravel, B. &. ((2005)). ATHENA, ARTEMIS, HEPHAESTUS: data analysis for X-ray absorption spectroscopy using IFEFFIT. *Journal of Synchrotron Radiation 12*, 537–541.

Ravel, B. (1997). Ferroelectric Phase Transitions in Oxide Perovskites Studied by XAFS, (PhD dissertation).

Rehr, J. e. (2010). Parameter-free calculations of x-ray spectra with FEFF9. *Phys. Chem. Chem. Phys., 12*, 5503-5513.

Sanson, A. (2010). Local dynamical properties of crystalline germanium and their effects in extended x-ray absorption fine structure. *PHYSICAL REVIEW B 81, 012304* .

Sayers, D., Stern, E. A., & Lytle, F. W. (1971). New Technique for Investigating Noncrystalline Structures: Fourier Analysis of the Extended X-Ray — Absorption Fine Structure*. *Physical Review Letters*, 1204-1207.

Vedrinskii, R. V. (1998). Pre-edge fine structure of the 3d atom K x-ray absorption spectra and quantitative atomic structure determinations for ferroelectric perovskite structure crystals. *J. Phys.: Condens. Matter 10*, 9561–9580.

CHAPTER 3

Experimental setup

The EXAFS data used in this thesis work has been acquired at the ESRF synchrotron situated in Grenoble. In this chapter we briefly outline the remarkable physical properties due to which synchrotron radiation is suitable for EXAFS spectroscopy and many other applications. Also, the beamline setting employed for this experiment is described along with the investigated MOFs samples.

3.1 Synchrotron radiation

3.1.1 X-ray sources

So far, we have seen the object of the investigation and the theory to understand the results of the experiment, but we still must introduce the experimental setup itself and in particular the source of X-rays to use. We have already given an idea of the typical energies necessary to observe the various atomic edges. Also, the spectra must be sampled very densely (a typical conventional value for the corresponding k-spacing is 0.05 Å^{-1}) in the high energy regime for up to around 2000 eV above the edge energy.

Having briefly outlined what is needed from the X-rays source, we must formalize it into suitable parameters and figures of merit. The first we present is the brilliance, which is a parameter that allows to relate performances of very different sources. It is defined as the radiation flux for unit of beam area, radiation bandwidth, beam divergence and is conventionally expressed in units of $\frac{photons}{s\cdot(mm^2)\cdot(mrad^2)\cdot(0.1\%\,BW)}$, which we will use in the following. This parameter is more relevant to experimental practice than for example simply the flux or the intensity of the beam because, as we will see later, the collimation of the beam and its spectral properties are crucial to the success of experiments.

To give an idea of the technological gap between cathodic tubes and third-generation light sources (which is the present one), we can observe that there is a difference of twelve

orders of magnitude in brilliance between typical X-ray tubes and that of the ESRF synchrotron (J. Als-Nielsen, 2001). The principal limiting factor for X-ray tubes is heat management at the anode, while in synchrotrons is the electron dynamics, so is dictated by magnetic fields, acceleration devices and control of the electron beam. Also, in X-ray tubes the photon energy of the fluorescence peaks (where the radiation is most intense) is not tunable and the radiation is not at all collimated from the source. There are also other parameters relevant to X-ray production and use, which are very particular to synchrotron operation, but before we can describe them we must see their underlying physics.

3.1.2 Synchrotron physics outline

A synchrotron is a particle accelerator which stores particle beams travelling at ultrarelativistic speed, that is $E \gg mc^2$. This is interesting for several reasons, depending on what particles are stored: synchrotron have been used to investigate high energy physics by accelerating protons, heavy ions, electrons and positrons, but if the interest is in producing electromagnetic radiation, electrons (and/or positrons) are more favourable. This derives from the fact that the power emitted from a charge accelerating depends heavily on its mass. As an example, we give an estimation of the power W emitted by irradiation from a particle in a (circular and ideal) synchrotron (Barone, 2004):

$$W \propto \left(\frac{E}{mc^2}\right)^4. \qquad (\mathbf{3.1})$$

It is then plausible to use electrons rather than heavier charged particles (e.g. protons) to produce intense radiation beams exploiting this phenomenon.

3.2 ESRF synchrotron

The data necessary to carry out the present analysis were collected at the European Synchrotron Radiation Facility (ESRF), situated in Grenoble. with the important caveat that those data refer to its working period contemporaneous to this thesis experimental work, while it is presently undergoing an update of its facilities. The storage ring is 844 m long in circumference and the electron energy of 6 GeV. Thus, for example, the radiation cone has an aperture $\Delta\theta \sim 0.08\ mrad$.

Figure 3.1: Aerial view of the ESRF ring, located near the confluence of the two rivers Drac and Isère. Photo retrieved from the ESRF web site: www.esrf.eu

In the following we will describe a typical bending magnet beamline, with reference to the BM23 and BM31 beamlines where the datasets have been collected. As for the BM23 beamline the magnetic field of the bending magnet is 0.85 T and the energy range is approximately from 5 to 75 KeV (The European Light Source Science and technology programme 2008-2017 ("Purple Book")).

3.2.1 Production of radiation

In a synchrotron circulating electrons, like the one at ESRF, their acceleration is achieved in several steps. First, electrons are accelerated into a linear accelerator, then they are inserted into a booster ring, where they are accelerated to the final speed, so that they can be passed to the storage ring, where they are kept circulating by means of resonant cavities while radiative losses occur. However, the electron beam must be "refilled" periodically to renew it.

3.2.2 Synchrotron radiation: Bending Magnet

What we describe in this section is usually denoted with the terminology 'Bending Magnet' (BM), but some properties will be valid for all synchrotron radiation. We therefore go on with the fundamentals of synchrotron radiation. As we have said before, the physical regime of the stored electrons is that of ultrarelativistic charged particles in a magnetic field.

The emitted radiation is characterized by power angular distribution, energy spectrum, polarization and temporal variability. In principle, these properties of the emitted radiation could be calculated from the electron current details. The results for a simple curving electron beam in a Bending Magnet (BM) along the line of sight tangent to the curving beam are essentially resumable as follows (J. Als-Nielsen, 2001), (Hofmann): as for the angular distribution, the main characteristic is the narrow radiation cone, with an opening angle proportional to $\gamma^{-1} = {m_e c^2}/{E}$. The spectral distribution is peaked near an energy value called Critical Energy $(E_c = \frac{3}{2}\frac{c\gamma^3}{\rho})$. For example, the ESRF critical energy at BM23 beamline is 21 KeV (Mathon & al., 2015). For $(E \ll E_c)$, the spectral distribution goes approximately as $E^{1/3}$, while for $(E \gg E_c)$, it decays exponentially with ${E}/{E_c}$.

Even if in the context of this thesis the polarization and the time dependency of the emitted radiation are not relevant, it is worth noticing that the synchrotron light is highly polarized on the plane of the synchrotron storage ring itself and that, as a consequence of the electron beam being in the ultrarelativistic regime and divided in bunches, the radiation is emitted in very short pulses (down to tenths of picoseconds). Also, the temporal variability due to beam decay and refilling might be relevant to experimental practice.

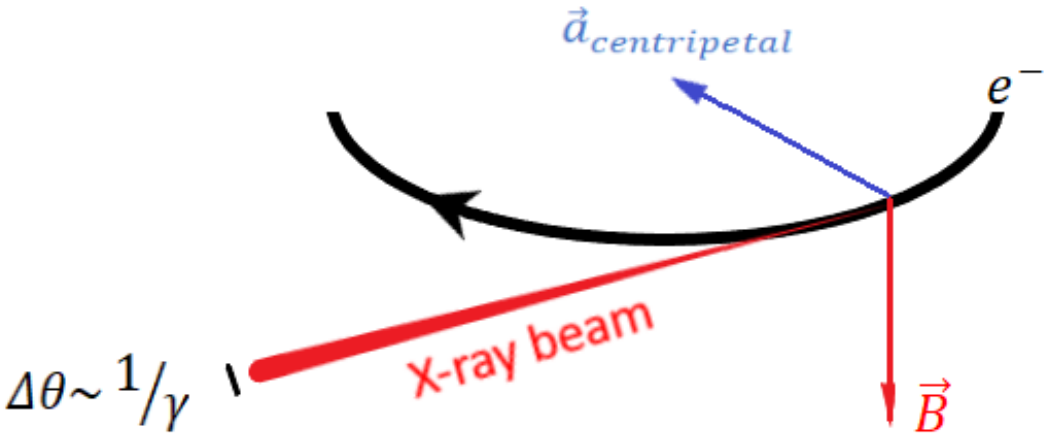

Figure 3.2: Synchrotron radiation emission in a bending magnet (not in scale): $\vec{B}$ represents the magnetic field, while $\vec{a}_{centripetal}$ the centripetal acceleration

3.2.3 Insertion devices

However, other possible configurations exist, where the difference among them is essentially regarding the magnetic configurations. As major examples we can cite the Wiggler and the Undulator. These are conventionally referred to as 'Insertion Devices' (ID). They are both composed of arrays of magnets.

The electron motion in this kind of magnetic field is oscillatory around the mean storage trajectory. During those oscillations, bremsstrahlung is emitted, and interference is established among the radiation deriving from the various oscillations. Thus, the resulting radiation is usually brighter than the one from a bending magnet and has a spectral distribution narrowly peaked around values depending on the spacing between magnets in the arrays (Hofmann).

From the above discussion we conclude that a bending magnet beamline (as BM23 and BM31 are) is a better choice for this kind of experiment, given the relative simplicity of operation and the overall effectiveness in stabilizing the radiation intensity with energy (due to their smoother spectral distribution).

3.3 Manipulation of radiation

3.3.1 Monochromator

Before the radiation can be let to incise on the samples, we must manipulate it to assure first its monochromaticity and that it is optimally focused and correctly orientated. So, the beam passes through slits, both vertical and horizontal, that ensure it has a certain starting width. There are various possible settings to obtain the monochromaticity of the radiation, depending on the specific requirements for the experiment ongoing.

The one used in our case is a double crystal monochromator, which consists of a couple of parallel single crystals exposing to the beam a certain crystalline plane. Exploiting Bragg reflection, by tuning the angle of incidence of the beam, it is then possible to isolate the chosen photon energy and let the filtered beam pass. Of course, there still are spurious frequencies in the so obtained radiation beam. These are mainly the higher harmonics of the selected frequency. To eliminate them, a rejection procedure must be applied, which is

usually by means of X-ray mirrors (the detuning of the angle of Bragg reflection could also be used to some extent if there are no mirrors).

As for the experiment described here, two different monochromator configurations were used (at each beamline). At BM23 beamline, the Zr K-edge energy (approximately 18 KeV) and the Ce L_3-edge (around 5.7 KeV) a Si (111) crystal has been used, while for the Ce K-edge (around 40 KeV) a Si (311) crystal was employed. At BM31, a Si (111) crystal was employed at Zr K, Ce L_3 and Ce K edges.

A possible configuration alternative to a double mirror monochromator is the polychromator, which consists of an X-rays mirror slightly bent towards the incident beam: in this way the various monochromatic components of the beam are separated on a suitable detector.

3.3.2 X-ray mirrors

Focusing and rejection of higher harmonics of the desired radiation are obtainable by means of an X-ray mirror, which is also effective in redirecting the beam. Since the real part of the refraction index for X-rays in most materials is lower, but very close to 1 (even less than one part in a million), a correspondingly narrow angle of incidence is needed to achieve total reflection (Bordiga & al., 2010).

However, in the described setting the mirrors were not used for focusing (i.e. they were flat at BM23 and there were no mirrors at BM31), but for the elimination of the higher harmonics satisfying Bragg's law and that if not eliminated could distort the measured data. As an illustrative example, in Table 1 some information about the mirror configuration at BM23 for the present work is given.

Beamline	Edge	Mirror used	Grazing angle [mrad]
BM23	Zr K	Rh coated	3
	Ce K	No mirrors	N/A
	Ce L_3	Silicon mirror	4.5

Table 3.2: Details of mirrors for BM23 as used for this thesis work

3.3.3 Experimental hutch

After passing through the optics hutch, the beam enters the experimental hutch, which is the place where the samples are located. Here the beam is let to incise on the sample as unperturbed as possible (let alone for the measurement processes on it). This is achieved through use of a vacuum pipe provided with a Kapton enclosure at its end, which usually confines with the sample environment.

A crucial step in the experimental setup is the very measurement procedure: it requires the measurement of the intensity of the radiation at certain points along its path. Depending on which kind of phenomenon or configuration is exploited to investigate the sample a different detector choice might be adopted (e.g. in fluorescence setup solid-state detectors might be preferred to ionization chambers due to the spatial configuration of the instruments).

For the transmission setup we are describing, ionization gas chambers were employed. This instrumentation is primarily composed by a controlled atmosphere space across which the radiation is let to pass. This causes ionization of the gas enclosed in the chamber, which is detectable through the induced current on high-voltage electrodes (e.g. 1 KV at BM31 ionization chambers used for this work).

To calibrate the energy scale for the experiment, a reference spectrum is usually acquired in series to the main sample. The control on the atmosphere composition is crucial for the success of the experiment. In fact, the gases generally must be changed upon change of work point, since their absorption properties are strongly dependent e.g. on incident photon energy.

Generally, a fixed fraction of the radiation is absorbed (at a certain energy) at each of the three ionization chambers, one before the sample (measuring I_0), one after the sample and before the reference sample (measuring I_t) and a last one after the reference. The mixture of inert (e.g. N_2) and/or noble (e.g. Kr, Ar, He) gases filling the chambers is chosen considering the absorption coefficient of the gases, but also the total pressure to be obtained (for example to avoid discharges in the chamber). To achieve this helium is used as it is practically transparent to the X-rays employed. Also, great attention must be used in cleaning the chambers from heavier gases when passing to lower energy edges. In Table 3.2 some technical details regarding the filling gases at BM23 and BM31 are reported.

Beamline	Edge	Before sample (I_0)	After sample (I_1)	After reference sample (I_2)
BM23	Zr K	Ar (0.4 bar) +He, Total pressure: 2 bar, 20% abs.@19 KeV	100% Ar, Total pressure: 2 bar, 70% abs. @19 keV	100% Ar, Total pressure: 2 bar, 70% abs. @19 keV
	Ce L_3	N_2 (0.2 bar) + He, Total pressure: 2 bar, 20% abs.@5.2 keV)	N_2 (1.13 bar) + He Total pressure: 2 bar, 70% abs at 5.2 keV	N_2 (1.13 bar) + He Total pressure: 2 bar, 70% abs at 5.2 keV
	Ce K	Kr (0.25 Bar) +He, Total pressure: 2 bar, 20% abs.@41 keV)	Kr (1.35 bar) +He, Total pressure: 2 bar, 70% abs. @41 keV	Kr (1.35 bar) +He, Total pressure: 2 bar, 70% abs. @41 keV)
BM31	Zr K	Ar (30%) +He, Total pressure: 1 bar, 15% abs. @17998 eV	Kr(10%) +Ar(90%), Total pressure: 1 bar, 70% abs. @17998 eV	Kr(10%) +Ar(90%), Total pressure: 1 bar, 70% abs. @17998 eV
	Ce L_3	N_2 (30%) +He, Total pressure: 1 bar, 18% abs. @5723 eV	Ar (10%) +He, Total pressure: 1 bar, 70% abs. @5723 eV	Ar (10%) +He, Total pressure: 1 bar, 70% abs. @5723 eV
	Ce K	Kr(15%) +Ar(85%) Total pressure: 1bar, 15% abs. @40443 eV	100% Kr, Total pressure: 1bar, 57% abs. @40443 eV	100% Kr, Total pressure: 1bar, 57% abs. @40443 eV

Table 3.3: Details of the filling gases in the ionization chambers for the samples under analysis in this work

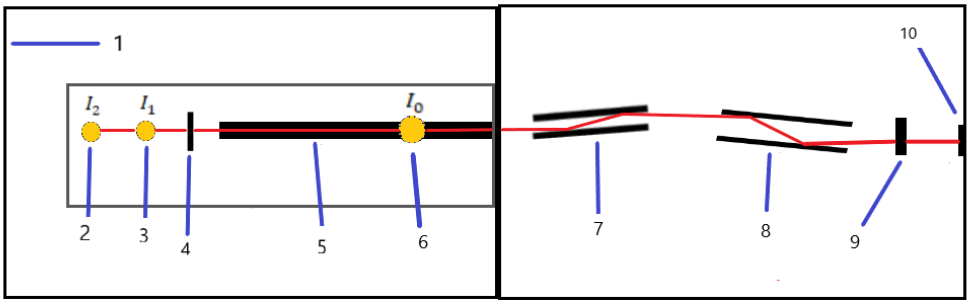

Experimental hutch

1 To the control room
2 Post-reference ion. chamber
3 Post sample ion. chamber
4 Sample holder
5 Vacuum pipe
6 Pre sample ion. chamber

Optical hutch

7 X-ray mirror
8 Monochromator
9 Primary slits (Front-End)
10 To the synchrotron

Figure 3.4: BM23 graphical description (not in scale), (Mathon & al., 2015). The optical hutch (on the right) is viewed from the side, while the experimental hutch (on the left) is viewed from above.

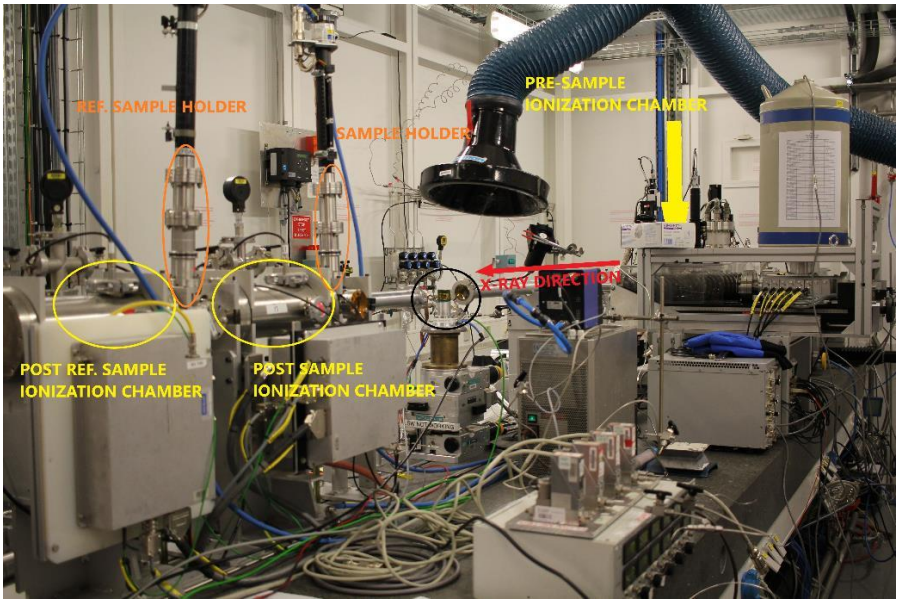

Figure 3.5: BM23 beamline experimental hutch photograph: above the vacuum pipe for X-ray transmission the X-ray beam direction is indicated by a red arrow, in orange the sample and reference sample holders, in yellow the ionization chambers. Inside the black circle in the center of the image another place for a sample holder is visible, where in the experiment described in this thesis a multiple-sample holder was placed, while this image refers to another experiment.

3.3.4 Sample environment

Further, there is a wide variety of possible environments in which the sample may be contained: (diamond) anvils, cryostats, furnaces, controlled atmospheres for chemical applications or to protect degradable samples (e.g. materials which cannot withstand open air) are usually disposable.

3.3.5 Samples presentation

The MOF samples were provided as powder by the group of Prof. Stock from Kiel University (see (Lammert & al., 2015) for a reference) and were moulded in self-supporting pellets of 5mm diameter by means of a mortar and a simple mechanical press, using BN (Boron Nitride) as filling agent for the ones employed in Ce L_3-edge measurements. Their mass was optimized by means of the XAFSmass software (Klementiev & Chernikov, 2016). Great cure has been provided to assure they were the most possible uniform and structurally stable, while also guaranteeing an optimal thickness. In fact, the signal to noise ratio must be as high as possible in the EXAFS region, and this is not possible if the contrast between the pre-edge and the post-edge region (usually quantified using the edge-step) is too small. Also, there is the necessity to let pass enough radiation to have a significant signal at the ionization chambers past the sample and past the reference. In Table 3, the MOF samples to be investigated are briefly presented.

Table 3.4: Summary of investigated MOF samples, with the Ce:Zr metallic ratio (estimated from EDX data)

Sample	Ce:Zr
Zr-UiO-66-Fum	Zr pure
Ce-UiO-66-Fum	Ce pure
Ce/Zr-UiO-66-Fum	10:90
	15:85
	31:69
	50:50
	83:17

Bibliography: Chapter 3

Barone, V. (2004). *Relatività: principi e applicazioni.* Bollati Boringhieri.

Bordiga, S., & al., e. (2010). X-ray absorption spectroscopies: useful tools to understand metallorganic frameworks structure and reactivity. *Chemical Society Reviews, 39*, 4885-4927.

Hofmann, A. (s.d.). *The Physics of Synchrotron Radiation.* Cambridge University Press.

J. Als-Nielsen, D. M. (2001). *Elements of Modern X-ray Physics.* John Wiley & Sons.

Klementiev, K.; Chernikov, R. XAFSmass: a program for calculating the optimal mass of XAFS samples. J. Phys.: Conf. Ser. 2016, 712, 012008.

Mathon, O., & al., e. (2015). The time-resolved and extreme conditions XAS (TEXAS) facility at the European SynchrotronRadiation Facility: the general-purpose EXAFS bending-magnet beamline BM23. *J. Synchrotron Rad., 22*, 1548–1554.

The European Light Source Science and technology programme 2008-2017 ("Purple Book"). (s.d.).

CHAPTER 4

Data analysis, results and discussion

In this chapter, a detailed description of the analysis of the acquired data is given, beginning from the structural models employed: the main model with two types of cornerstones per cerium concentration and a secondary model in which metallic sites in the cornerstones are randomly occupied. Then, the pre-processing procedures of the acquired data are described, and the fits are presented along with a discussion of their significance for the modelization of the MOFs.

4.1 Path degeneration in bimetallic Ce/Zr-UiO-66 MOFs

As mentioned before during the description of the EXAFS equation, the N_{path} parameters (coordination number) are the crucial aspect of the material modelization performed on the bimetallic MOFs. In fact, by formulating a hypothesis about the distribution of the population of cornerstones among the possible metallic configurations, which we report again here in Figure 4, it is possible to infer the coordination number and, through a fitting procedure for the EXAFS signals, validate or reject it.

The general formula for expressing the coordination numbers as functions of the total metallic fraction in the sample (we will use that of cerium without loss of generality) is:

$$N_{path,[Ce]} = \frac{\sum_i N_{paths,i} \cdot f_{i,[Ce]}}{\sum_i N_{abs,i} \cdot f_{i,[Ce]}}, \qquad (\mathbf{4.1})$$

where the index i runs over the cornerstone types present in the MOF at the selected cerium concentration, $N_{paths,i}$ stands for the number of paths of the type $M \rightarrow M$ (with M=Zr,Ce) (for which the degeneration is calculated) in the cornerstone of type i, $N_{abs,i}$ stands for the number of the absorber atoms in a certain cornerstone type, $f_{i,[Ce]}$ represents

the fraction of cornerstones of type i at a certain cerium concentration. For the sake of completeness, the paths for the second atomic shell are represented pictorially in Figure 2.

To motivate this formula, we must remember the definition of the EXAFS signal $\chi(k)$, which informally can be seen to depend on the path configurations in its numerator, while in the denominator the dependence is on the atomic content of the cornerstones. Also, the various combinatorial factors counting the paths and the atoms are weighted with the cornerstone fractions because of the local nature of EXAFS, which makes of the cornerstones the effective material unit from its point of view.

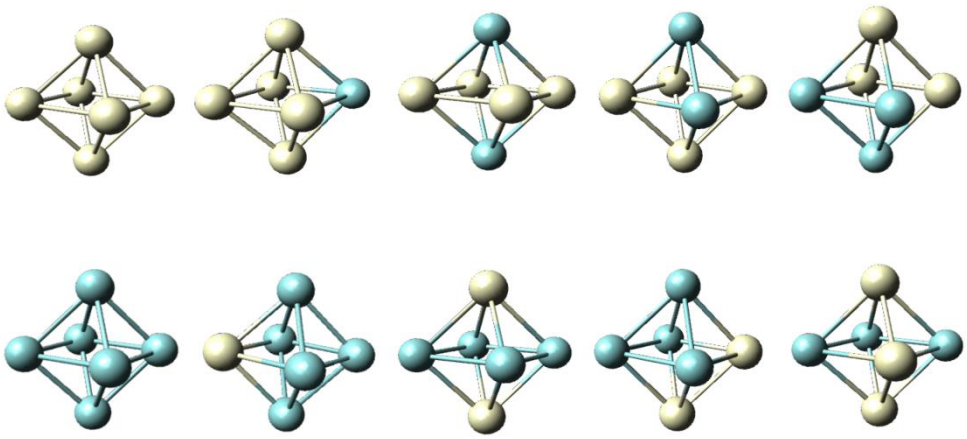

Figure 4.1: All the possible metallic stoichiometric configurations for the bimetallic octahedral UiO-66 cornerstones. In the model with randomized composition, all of these are (in principle) present, while for the other one, just the first two on the left and the second from left of the first row

Table 4.5: Coordination numbers derived from the model featuring only two types of cornerstones at a single Cerium fraction

Ce:Zr ratio	$N_{Zr\to Zr,tot}$	$N_{Zr\to Zr,par}$	$N_{Zr\to Ce}$	$N_{Ce\to Zr}$	$N_{Ce\to Ce}$
Pure Zr	4	0	0	0	0
10:90	1.78	1.78	0.44	4	0
15:85	0.47	2.83	0.71	4	0
31:69	0	3.2	0.8	1.78	2.22
50:50	0	3.2	0.8	0.8	3.2
83:17	0	3.2	0.8	0.16	3.84
Pure Ce	0	0	0	0	4

We will use (and confront) two stoichiometric hypotheses. In the first one, there are two $[Ce]$ regimes: one for $[Ce] < {}^{1}/_{6}$, the other for $[Ce] > {}^{1}/_{6}$. In the former the only cornerstones allowed are those with all six vertices occupied by zirconium atoms and with five vertices by zirconium and one by cerium, while in the latter those with all six vertices occupied by cerium atoms and with five vertices by zirconium and one by cerium (Lomachenko & al., 2018).

In the second one (which will serve as a null hypothesis) the population of the metallic sites is randomized, i.e. all the six metallic sites have the same probability of being occupied by a metallic atom of a certain type. The results are shown in Tables 4.2 & 4.3, ordered by relative path and actual metallic ratio as in the analysed samples.

Table 4.6: Coordination numbers derived from the stoichiometric model assuming the cornerstones are randomly occupied by Cerium and Zirconium atoms

Ce:Zr ratio	$N_{Zr \to Zr}$	$N_{Zr \to Ce}$	$N_{Ce \to Zr}$	$N_{Ce \to Ce}$
Pure Zr	4	0	0	0
10:90	3.6	0.4	3.6	0.4
15:85	3.4	0.6	3.4	0.6
31:69	2.76	1.24	2.76	1.24
50:50	2	2	2	2
83:17	0.68	3.32	0.68	3.32
Pure Ce	0	0	0	4

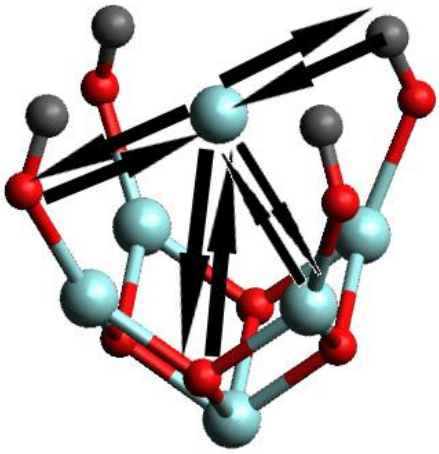

Figure 4.2: Pictorial representation of some single scattering paths for the investigated cornerstone.

The reason behind this choice is that the two models will be shown to have the same number of free parameters, thus allowing for a statistical comparison. Also, it is remarkable that they exhibit no free parameter regarding the coordination numbers. This is to be confronted with models allowing more than two cornerstones in the same sample, which have $(N-2)$ more free parameters in the coordination numbers, where N is the number of cornerstone types.

Calculating the $f_{cornerstone}$ as a function of the $[Ce]$ is straightforward for this first (and main) model. In fact, the following simple system of equations holds:

$$\begin{cases} [Ce] + [Zr] = 1 \\ 6 \cdot f_{tot} + 5 \cdot f_{par} = 6 \cdot [Zr] \\ f_{par} = 6 \cdot [Ce] \end{cases} \quad for\ [Ce] < {}^{1}/_{6} \qquad (\mathbf{4.2})$$

$$\begin{cases} [Ce] + [Zr] = 1 \\ 5 \cdot f_{par} = 6 \cdot [Zr] \\ 6 \cdot f_{tot} + f_{par} = 6 \cdot [Ce] \end{cases} \quad for\ [Ce] > {}^{1}/_{6} \qquad (\mathbf{4.3})$$

It is remarkable that the formula above satisfies the usual constraint $\sum_{Scatt} N_{Abs \to Scatt,shell} = \#_{shell}$, where $\#_{shell}$ stands for the number of atoms in the inspected shell, which in the case of this work is 4 (the metallic atoms in the square in the mid of the cornerstone octahedron). On a more practical side, the total metallic fraction $[Ce]$ is the parameter controlled at synthesis level.

As can be seen from the relative tables (4.2 & 4.3), the coordination numbers are neatly different for the two models, so it is plausible to think that they can be well-distinguished by looking at their fit results.

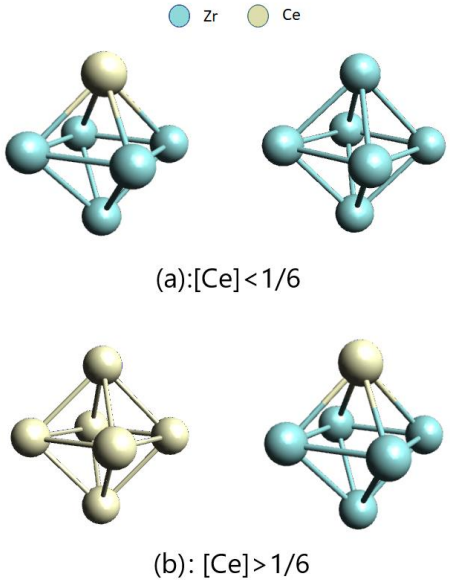

Figure 4.3: Representation of the cornerstone content as in the model with only two cornerstones.

4.2 Analysis of the MOFs EXAFS spectra

In the following, we will deepen the details about the analysis of the acquired datasets. All the fitting procedure has been conducted using the Demeter software package (Ravel, (2005)). The starting physical point will be the structural information about the Zr-UiO-66 and Ce-UiO-66 cornerstones available from diffraction studies of the material (see for example (Lomachenko & al., 2018). Also, a fitting model will have to be formed by introducing reasonable constraints between fitting parameters for the datasets at different cerium fractions, edges and beamlines. But first, we must briefly summarize what the datasets are and consider the pre-processing procedure more in detail.

4.2.1 Samples and datasets

For every MOF sample (i.e. for each of the Ce:Zr ratios) a set of at least three spectra was acquired at each of cerium K (40443 eV), zirconium K (17998 eV) and cerium L_3 (5723 eV) edges. The spectra were acquired at the beamlines BM23 and BM31 at ESRF.

4.2.2 Pre-processing procedure: Zr K and Ce L_3 edges

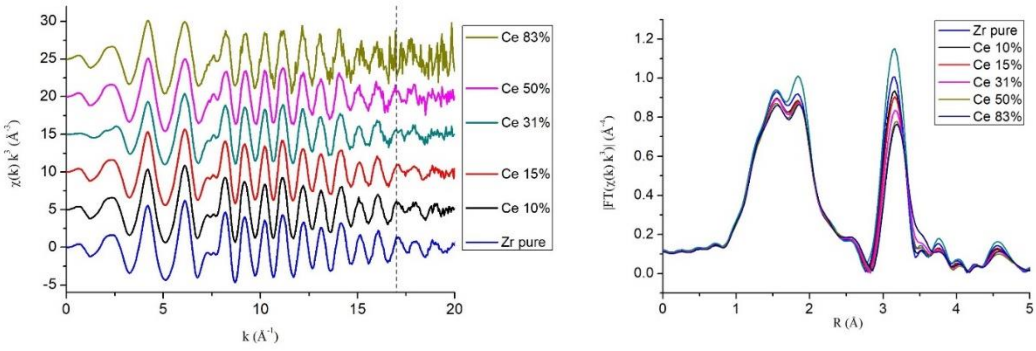

Figure 4.4: EXAFS signals for Zr K edge weighted with a k^3 factor (left) and the magnitude of the relative Fourier transform, using the signal in the k range [3.7-17], with the k^3 factor weight and Hanning windows.

Considering Zr K edge and Ce L_3 edges, the pre-processing procedure was performed in the following way. The energy scale calibration and alignment of the reference sample

spectra was performed on every set of spectra from the same sample at the same edge. The (lowest) energy of maximum absorption of the reference samples spectra was defined as the edge energy and the reference spectra themselves aligned consequently. In Figure 7 the EXAFS signals relative to Zr K edge extracted and weighted are shown together with the magnitude of their Fourier transforms is presented. The Ce L_3 edge XANES spectra are shown in Figure 4.6 but were not used for EXAFS analysis.

4.2.3 Pre-processing procedure: Ce K edge

Regarding Ce K edge, the datasets were grouped in a similar way, but the procedure itself had to be performed in a different way, due to the noise in the XANES region of the spectra acquired at BM31 (i.e. those with $[Ce] > 17\%$), that prevented an accurate individuation of the point of maximum absorption. Since it is plausible that the low energy resolution of the monochromator is the cause of such a behaviour, the positions of the maxima of the absorption have instead been considered reliable as references and as such the spectra were aligned at them. The EXAFS signals are shown in Figure 4.5, together with the magnitude of their Fourier transforms is presented.

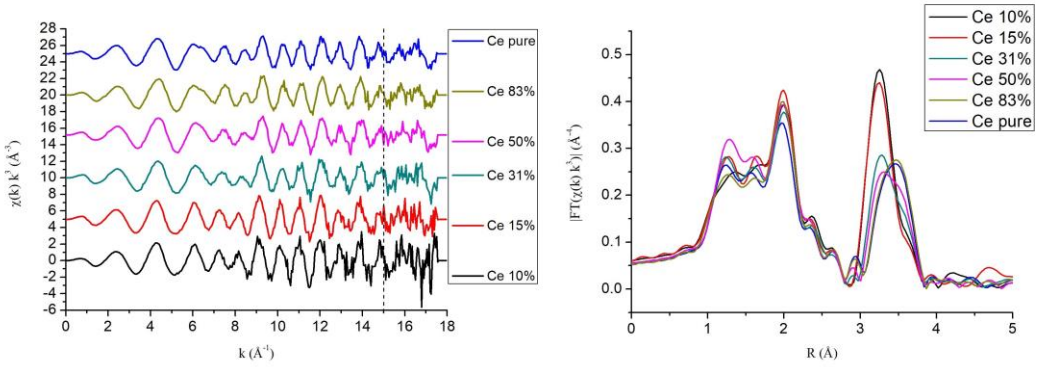

Figure 4.5: EXAFS signals for Ce K edge weighted with a k^3 factor (left) and the magnitude of the relative Fourier transform, using the signal in the k range [3.7-15], with the k^3 factor weight and Hanning windows.

4.3 XANES qualitative analysis

A first kind of analysis has been performed on the XANES region of the acquired spectra at Ce L_3 edge. Its goal is to ascertain the oxidation state of the cerium contained in the MOF samples. It consists in a qualitative observation of the spectra, exploiting the fact that XANES part of the absorption for $Ce(III)$ and $Ce(IV)$ are distinguishable by well-defined structural features. In fact, $Ce(IV)O_2$ presents two peaks, while $Ce(III)NO_3$ only one at slightly lower energy. The MOF samples and the XANES references for both oxidation states ($Ce(III)NO_3$ and $Ce(IV)O_2$) are shown in Figure 4.6. From this comparison it may be inferred that the cerium present in the MOFs is mostly in the Ce(IV) form, while the Ce(III) is at most some percent (Smolders & al., 2018): this is important due to the fact that in UiO-66 cerium atoms are (normally, see for example (Smolders & al., 2018)) in Ce(IV) form.

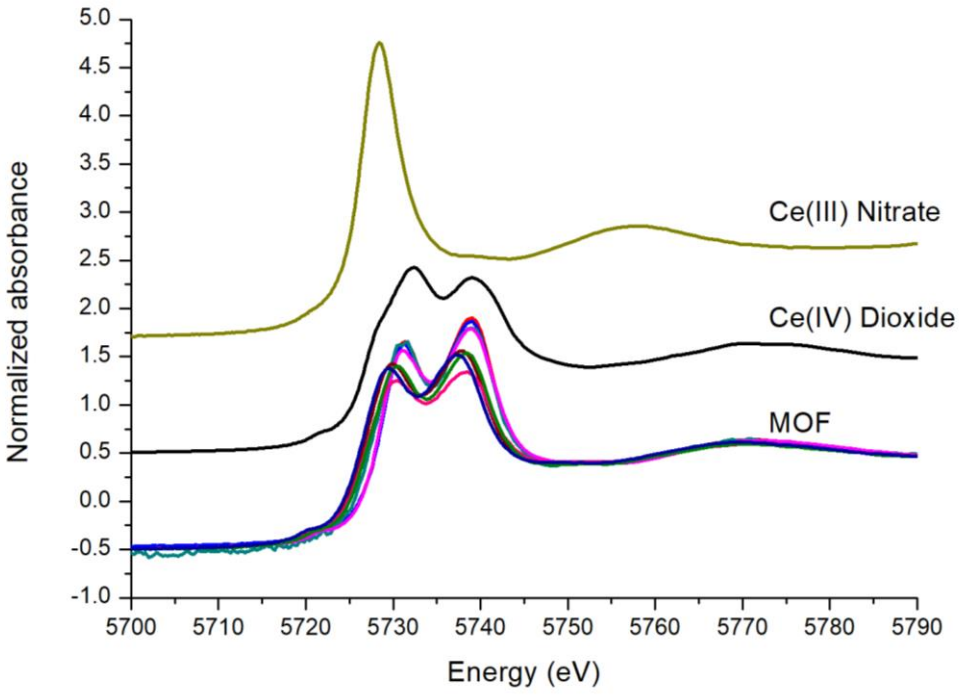

Figure 4.6: XANES region of the spectra at Ce L_3 edge for the MOF samples and the reference samples with Ce(IV) and Ce (III)

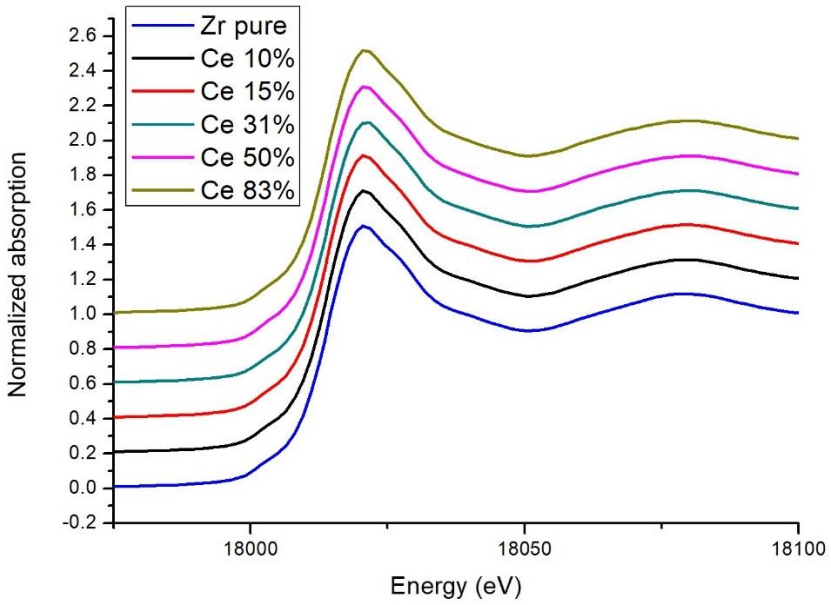

Figure 4.7: XANES region of the MOFs spectra at the Zr K edge

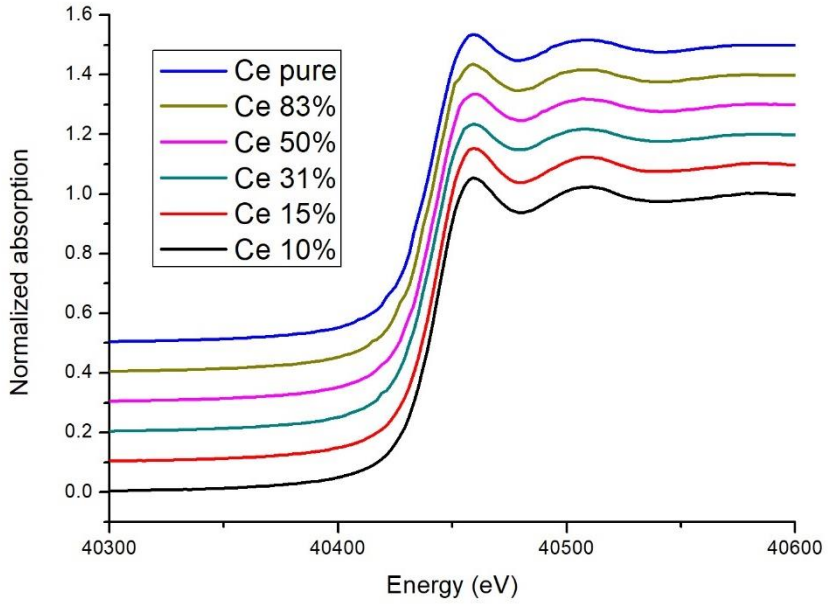

Figure 4.8: XANES region of the MOFs spectra at the Ce K edge

Also, regarding the XANES regions of the MOFs spectra at Zr and Ce K edges, shown in Figures 4.7 and 4.8, it can be said that they are very similar, thus allowing to conclude that the local coordination geometry and electronic structure cannot be strongly dependent on the Ce:Zr ratio. This will be useful during the parametrization of the EXAFS fitting curve, since will allow to use only

one S_0^2 parameter per each edge. As a final remark, the XANES signals are also useful to help excluding the presence of extra phases in the investigated MOFs samples.

4.5 Compatibility of different beamlines data

We note however that the two beamlines have employed a different setup, in particular regarding the monochromator used at the cerium K edge. Thus, we will have to assure that the datasets acquired at different beamlines are compatible with each other. To do this in a practical way, we will find empirically a relationship between the EXAFS fitting parameters for well-known and well reproducible samples for both cerium K edge and zirconium K edge and use it as a constraint in the EXAFS fitting procedure for MOF samples. The reference samples used are CeO_2 for cerium and ZrO_2 for zirconium. The fit curves imposed over data points are visible in Figure 4.9.

The result of this analysis is that all EXAFS fitting parameters are equal for the two beamlines within statistical uncertainty apart some of the Debye-Waller factors for Ce K edge spectra. A reasonable constraint relating the Debye-Waller factors relative to paths present both in spectra from BM23 and BM31 is $\sigma^2_{BM31} - \sigma^2_{BM23} = 0.0002$ Å^2, therefore not so significant for the fits.

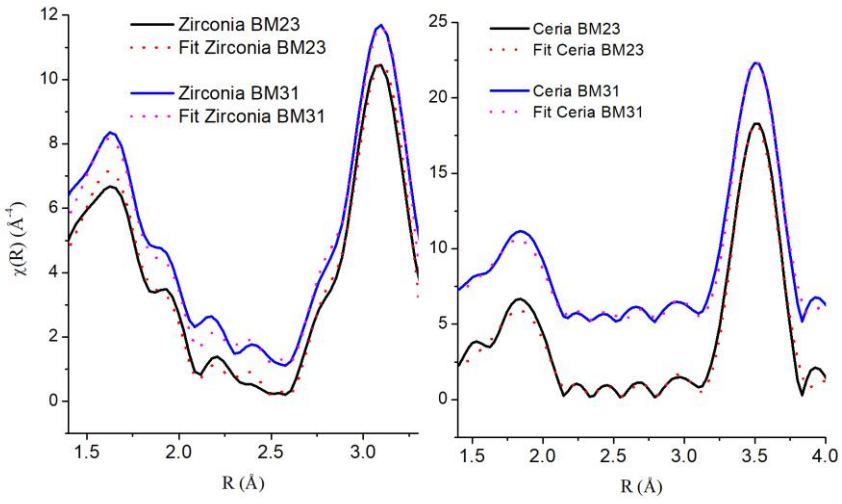

Figure 4.9: EXAFS fit for the zirconium and cerium dioxides at the two different beamlines

4.6 Main model examination

Having established a reasonable relationship between BM23 and BM31 data in the form of relations between EXAFS fitting parameters, we advance in elaborating and motivating the EXAFS fitting model for the two cornerstones model. All the 12 datasets were fitted altogether using as scattering paths only the single scattering paths involving metal atoms of the second shell. A pictorial representation of some of the single scattering paths for the investigated cornerstones is shown in Figure 4.2. Thus, only the following paths are considered: $Ce \rightarrow Ce, Ce \rightarrow Zr, Zr \rightarrow Ce$ and $Zr \rightarrow Zr$. Also, the coordination numbers are imposed to be those given in the second chapter of this thesis for this model. The detail of the fitted data can be seen in Figure 4.10 and 4.11. It is worth to stress that the strong variation of the EXAFS signals with Ce:Zr ratio implies that mixed-metal cornerstones are present in the material: if they were not, the local neighbourhood of metal atoms would be unchanged with Ce:Zr ratio and the EXAFS signals at each edge would also be unchanged.

Before passing on to the parametrization of the EXAFS fitting curve, a qualitative interpretation of the EXAFS signals for the point of view of the preferential cornerstones' formation model can be given. In fact, looking at the magnitudes of the Fourier transforms, a remarkable shift of the peaks towards higher R values may be seen at Ce K edge and not at Zr K edge. This fact is well understandable in the considered model: the mean Zr-Zr and Zr-Ce distances are seen for every Ce:Zr ratio at the Zr K edge, while at Ce K edge only from a certain Ce:Zr ratio the mean Ce-Ce distance (greater than the Ce-Zr one) begins to appear. Also, the intensity of the signals at Zr K edge diminishes with increasing Ce:Zr ratios without great change in position of the peaks, again reinforcing the idea that only a stoichiometric change in proportion of cornerstone types is responsible for the variation of the signals with Ce:Zr ratios.

In principle this model requires for each path a Debye-Waller factor and a ΔR, which is defined as the difference between first cumulant and half of the path length (in case of single scattering paths this may be interpreted as the distance between absorber and back-scatterer) and an amplitude S_0^2 and an edge energy correction ΔE_0 for each absorber type and for each dataset, all of which would be distinct and fitted independently. Anyway, most of these independent parameters are not necessary to obtain a significant fit. In fact, their

number can be significantly reduced by considering some physical properties of the investigated samples.

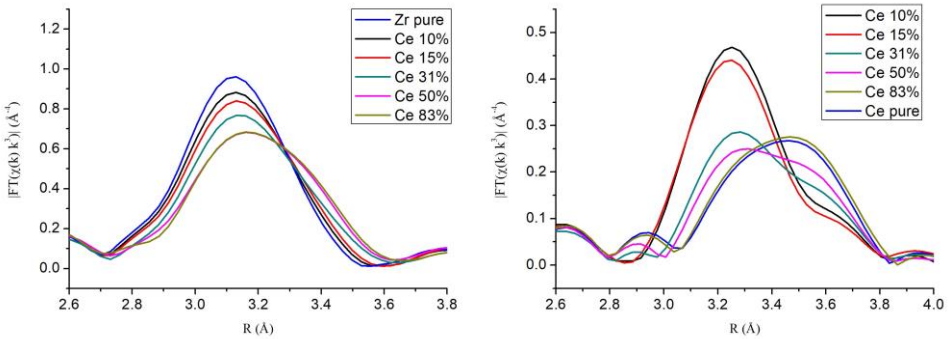

Figure 4.10: Detail of the magnitude of the Fourier transform for second shell signal in R space, obtained using the k-range [3.7-15] for Ce K edge and [3.7-17] for Zr K edge.

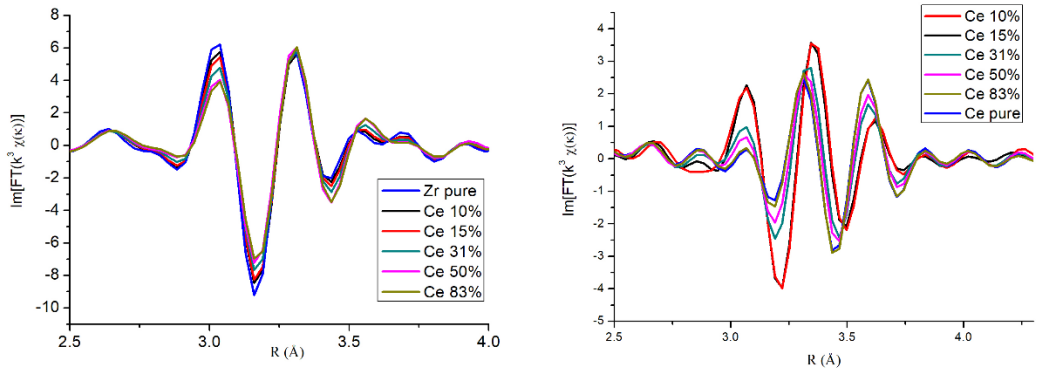

Figure 4.11: Detail of the imaginary parts of the Fourier transform for second shell signal in R space, obtained using the k-range [3.7-15] for Ce K edge and [3.7-17] for Zr K edge.

The amplitudes S_0^2 and the edge energy corrections ΔE_0 surely must be distinct for Zr and Ce absorbers, but they can be considered equal for all the datasets from samples of different Ce:Zr fraction. This is physically motivated since the change in cerium fraction is not expected to strongly modify the physical properties of the metallic atoms: in fact, the main effect of the change in Ce:Zr fraction is expected to be a stoichiometric modification of the cornerstone composition of the MOF, while the cornerstones themselves maintain their structure.

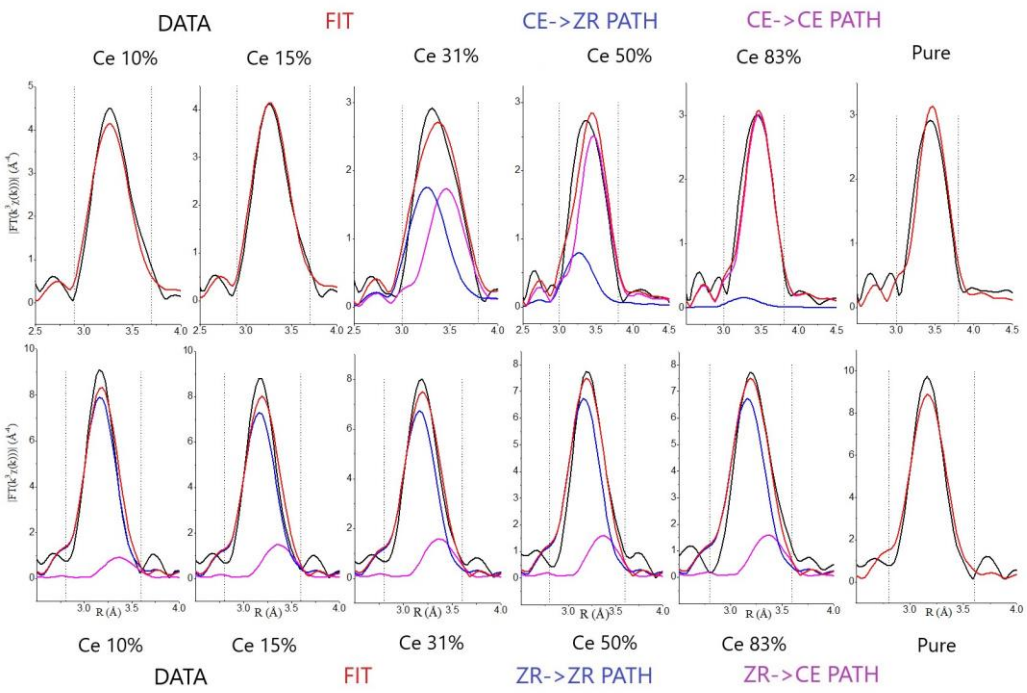

Figure 4.12: A compact presentation for the fitted data. In the upper row are the Ce K edge signals, in the lower the Zr K edge ones.

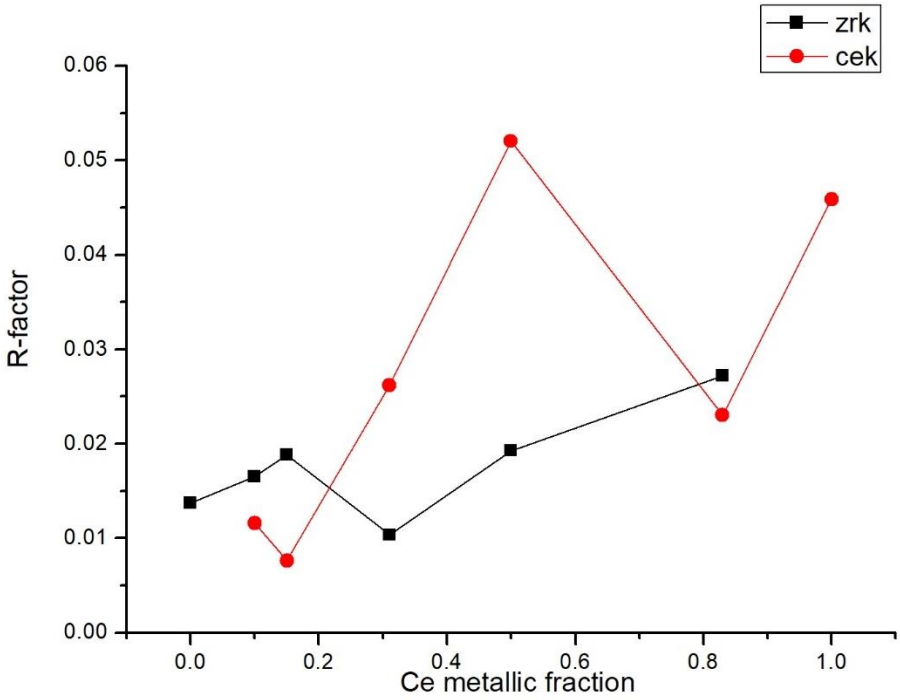

Figure 4.13: R-factors for the single datasets presented above fitted with the preferential cornerstones' formation model using the k-ranges from 3.7 Å^{-1}

$S^2_{0,Zr}$	(0.92 ± 0.03)
$S^2_{0,Ce}$	(1.02 ± 0.02)
$E_{0,Zr}$	$(0.5 \pm 0.2)\ eV$
$E_{0,Ce}$	$(1 \pm 2)\ eV$
$R_{Zr \to Zr}$	(3.518 ± 0.003) Å
$\sigma^2_{Zr \to Zr}$	(0.0043 ± 0.0001) Å^2
$R_{Zr \to Ce}$	(3.664 ± 0.003) Å
$\sigma^2_{Zr \to Ce}$	(0.0047 ± 0.0002) Å^2
$R_{Ce \to Ce}$	(3.793 ± 0.006) Å
$\sigma^2_{Ce \to Ce}$	(0.0060 ± 0.0001) Å^2
Global R factor	(0.024 ± 0.001)
Global reduced χ^2	(305 ± 17)
Maximum R factor	0.052 (Ce K edge-Ce 50%)
Minimum R factor	0.008 (Ce K edge-Ce 15%)
N_{DoG}	71

Table 4.7: Best fit parameters for the EXAFS signals fitted with a k range [3.7:15] for Ce K edge and [3.7:17] for Zr K edge, obtained employing the main stoichiometric model

The various ΔR and σ^2 parameters are also expected to be independent of the Ce metallic fraction and this reduces them to one for path type, except for those relative to the $Ce \to Zr$ and $Zr \to Ce$ paths, which are constrained to be the same. Also, the $\Delta R_{Zr \to Zr}$ and $\sigma^2_{Zr \to Zr}$ parameters are assumed to be the same for Zr_6 and $CeZr_5$ cornerstones. The distance between Zr atoms in a pure cornerstone is assumed as 3.51 Å, while for the pure cornerstone of cerium is 3.78 Å from X-ray diffraction study of the MOFs (Lomachenko & al., 2018). Fit results are reported in Table 4.3 and in Figure 4.12 to let comparison of structural properties with the fit settings that we will see in the rest of the chapter. Reported uncertainties related to mean best fit values are calculated as root mean square of the values for the various datasets fitted independently.

4.7 Optimal k-ranges evaluation

However, the EXAFS analysis performed in this way is not satisfactory on a quantitative level (even if it shows a qualitative agreement of data with the model). The major problem resides in the high number of atoms (that is the oxygen and carbon atoms near the metallic absorber) which are not taken into consideration and must be introduced also in multiple scattering paths. This approximation is very simplistic but may be reasonable if the only interest of the analysis resides in the stoichiometry of metals in the cornerstones. To evaluate the optimal k-range the amplitudes of the considered metallic paths were compared to the scattering with oxygens on the opposite faces of the cornerstone with respect to the absorber, that is the most important other single scattering for second shell. The relative scattering amplitudes are reported in Figure 4.14, computed using FEFF8 (Ankudinov & al., 1998).

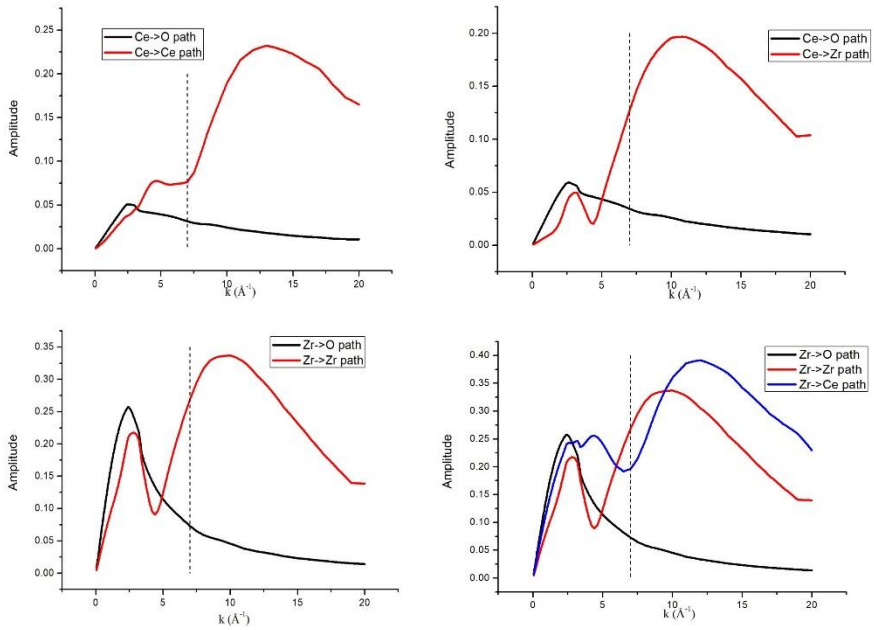

Figure 4.14: Amplitudes of the considered metallic paths reported with the amplitude of the main other single scattering path at second shell (with oxygen). The dashed line represents the cut-off in k used for the second fits.

The fit results with this different k-range are reported in Table 4.4. In Figure 4.15 a compact presentation of fits is given, while in the following figures (4.16-4.21) the fits for every cerium concentration are reported. Reported uncertainties related to mean best fit

values are calculated as root mean square of the values for the various datasets fitted independently.

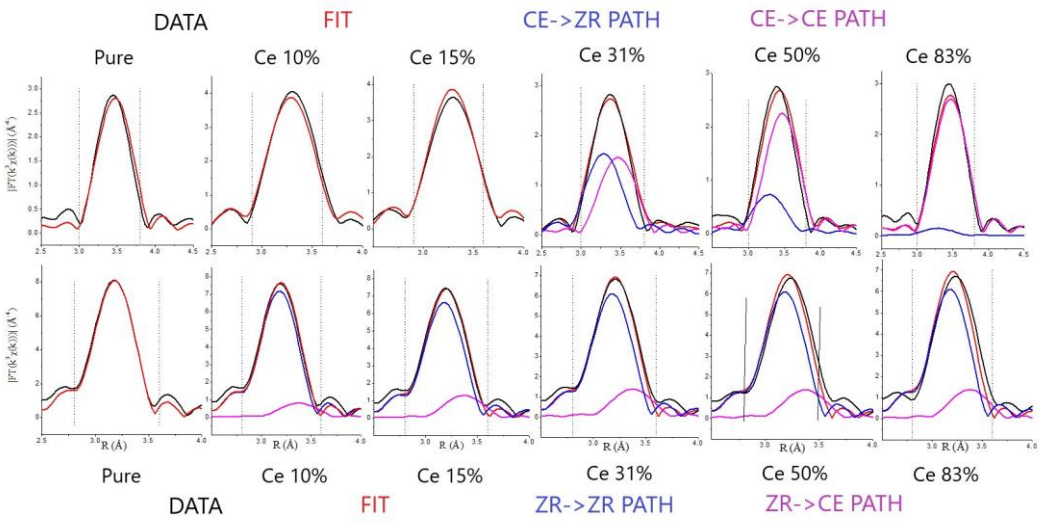

Figure 4.15: Compact presentation of the EXAFS fits for the main stoichiometric model for data in the k-range [7-15] for Ce K edge and [7-17] for Zr K edge. In the upper row are the Ce K edge signals, in the lower the Zr K edge ones.

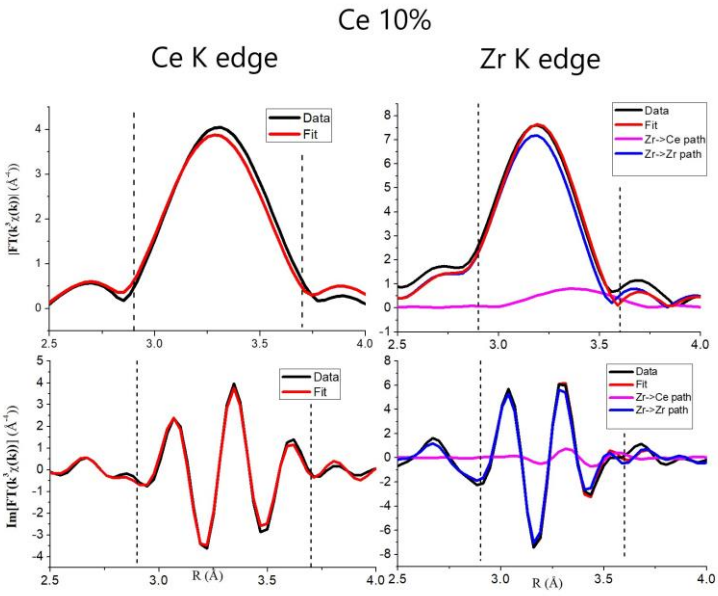

Figure 4.16: Best fit for MOF with [Ce]=10%.

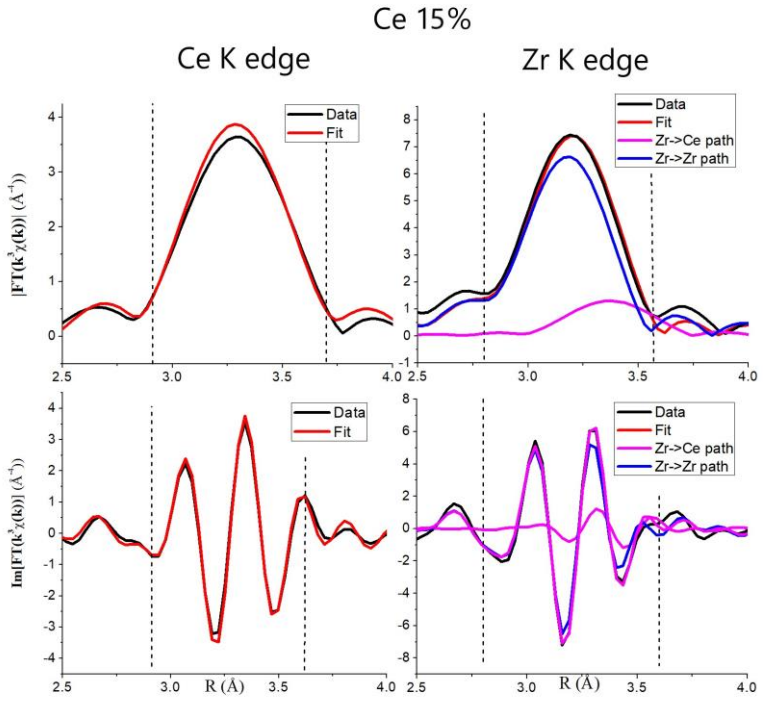

Figure 4.17: Best fit for MOF with [Ce]=15%.

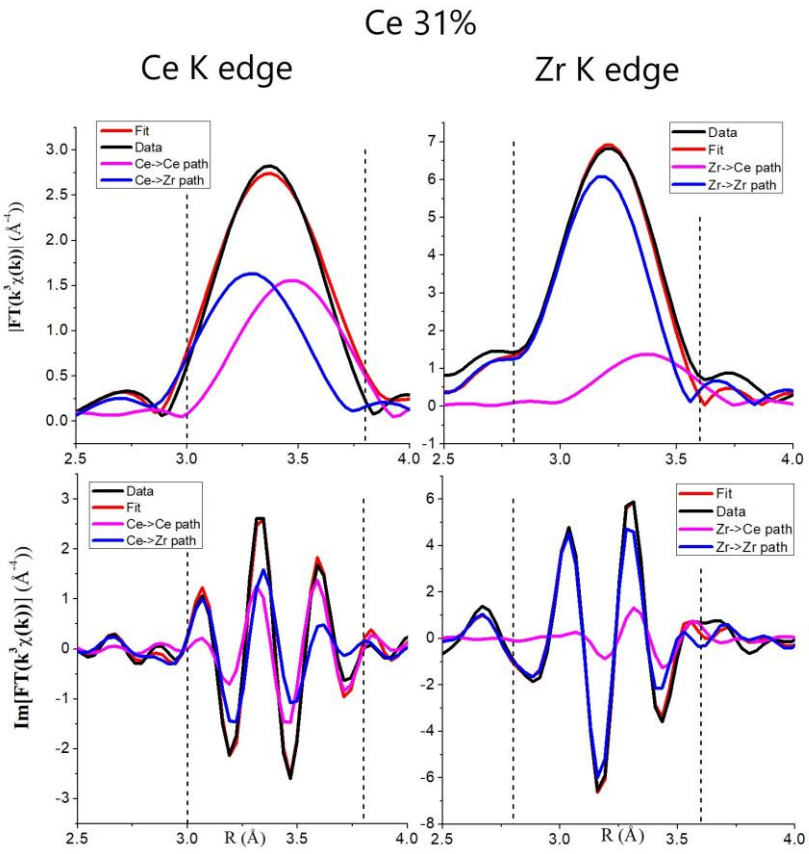

Figure 4.18: Best fit for MOF with [Ce]=31%.

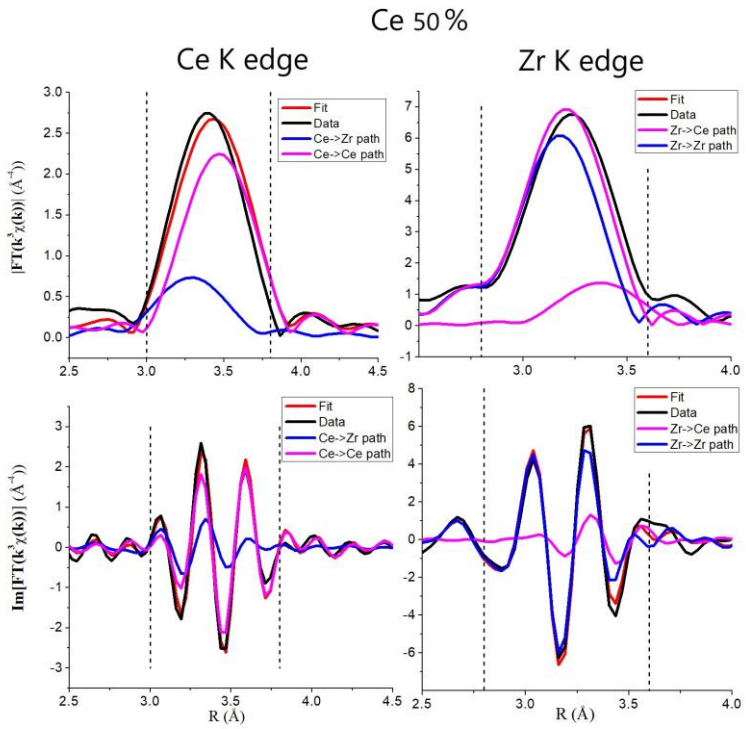

Figure 4.19: Best fit for MOF with [Ce]=50%.

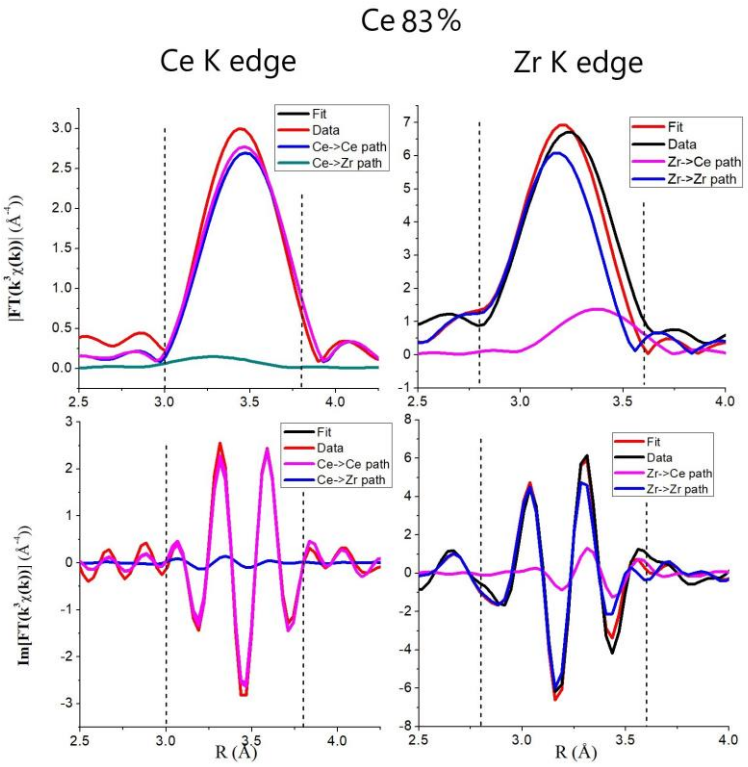

Figure 4.20: Best fit for MOF with [Ce]=83%.

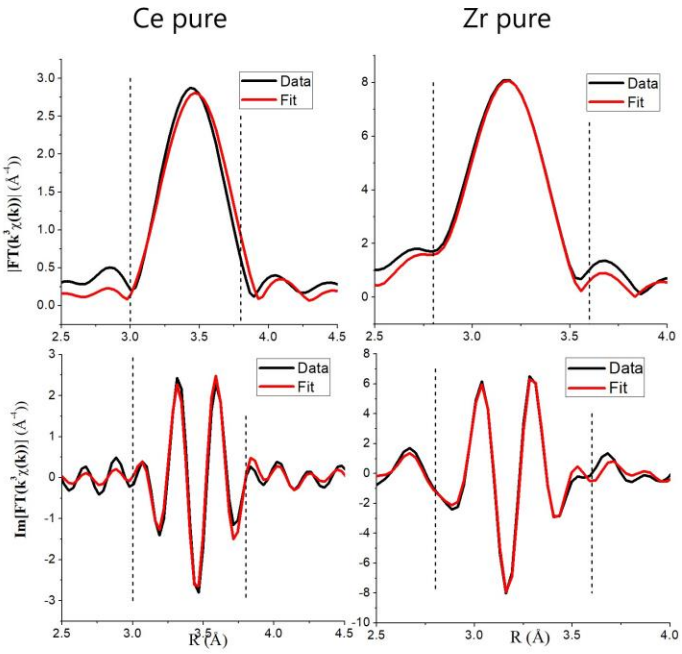

Figure 4.21: Best fit for monometallic MOFs.

$S^2_{0,Zr}$	(0.84 ± 0.02)
$S^2_{0,Ce}$	(1.00 ± 0.05)
$E_{0,Zr}$	$(-0.5 \pm 0.2)\ eV$
$E_{0,Ce}$	$(1 \pm 2)\ eV$
$R_{Zr \to Zr}$	(3.515 ± 0.003) Å
$\sigma^2_{Zr \to Zr}$	(0.0040 ± 0.0001) Å^2
$R_{Zr \to Ce}$	(3.665 ± 0.002) Å
$\sigma^2_{Zr \to Ce}$	(0.0047 ± 0.0003) Å^2
$R_{Ce \to Ce}$	(3.794 ± 0.004) Å
$\sigma^2_{Ce \to Ce}$	(0.0059 ± 0.0002) Å^2
Global R factor	(0.0133 ± 0.0003)
Global reduced χ^2	(180 ± 9)
Maximum R factor	0.03 (Ce K edge-Ce 50%)
Minimum R factor	0.006 (Zr K edge-Ce 31%)
N_{DoG}	52

Table 4.8: Best fit parameters for the EXAFS signals using the signal in the k-range [7:15] for Ce K edge and [7:17] for Zr K edge, obtained employing the main stoichiometric model.

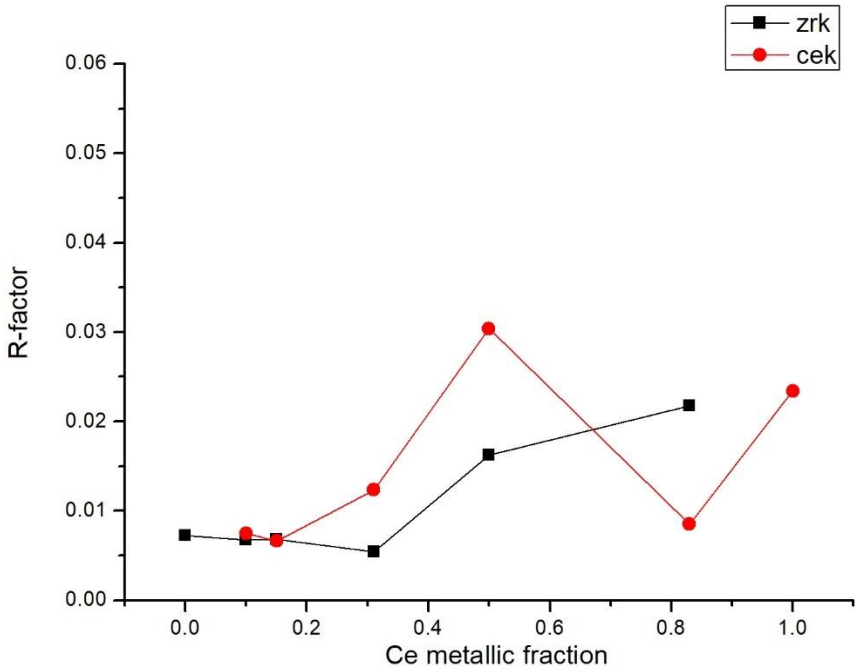

Figure 4.22: R-factors for the single datasets presented above fitted with the preferential cornerstones' formation model using reduced k-ranges

4.8 Random formation model

In view of the weaknesses the model may exhibit by neglecting such a great number of possible physical sources of EXAFS signal, we want to show that this model fits data better than a model built relying on a null hypothesis, which consists in the random formation of cornerstones. The fitting model is formally similar to the previous one, but presents several differences: first of all, the coordination numbers and also the presence of all types of paths for every spectrum (apart from those from samples containing only one type of metal). For the rest the model still employs the same parameters as the one used above. This allows a reasonable comparison between the two systems, since as already mentioned in the second chapter, they have the same number of degrees of freedom. A compact presentation of the fits is given in Figure 4.23, while in Table 4.5 the parameters relevant for the fit quality are reported. Reported uncertainties related to mean best fit values are calculated as root mean square of the values for the various datasets fitted independently.

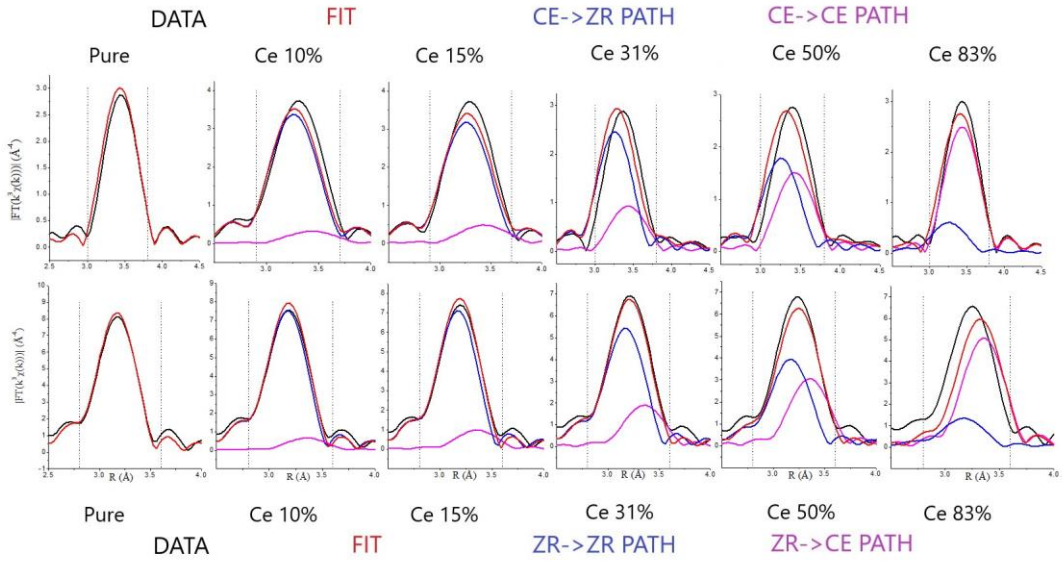

Figure 4.23: Compact presentation of the EXAFS fits employing the random formation model

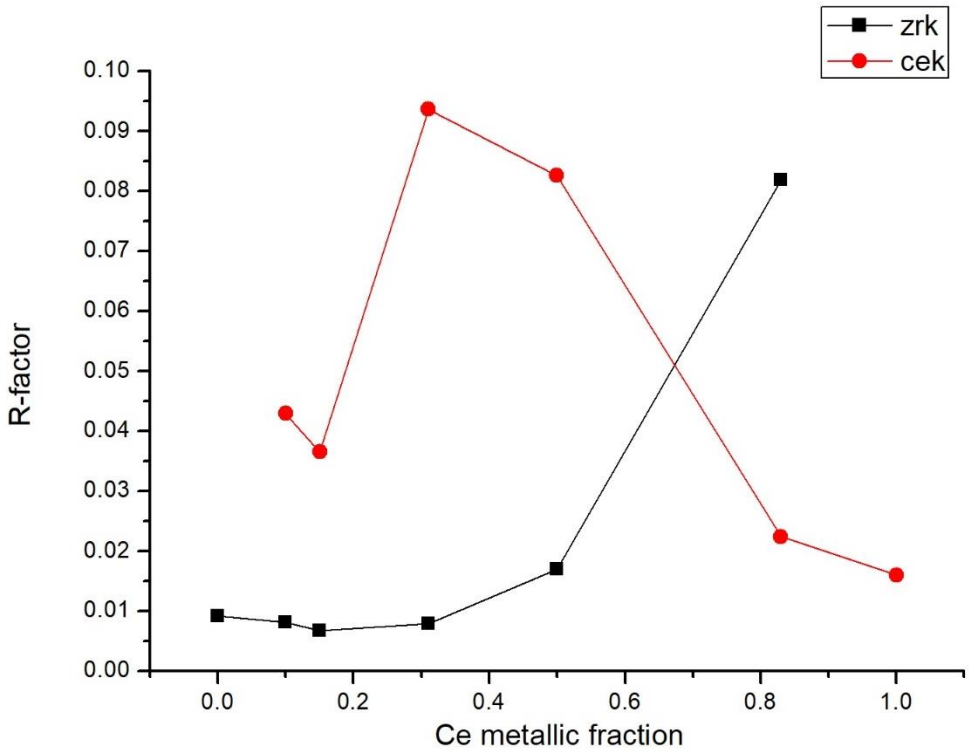

Figure 4.24: R-factors for the single datasets presented above fitted with the random cornerstones' formation model using the reduced k-ranges

Global R factor	0.035
Global reduced χ^2	268
Maximum R factor	0.094 (Ce K-Ce 31%)
Minimum R factor	0.007 (Zr K-Zr pure)
N_{DoG}	52

Table 4.9: Excerpt of best fit parameters for EXAFS signals in the k range [7-15] for Ce K edge and [7-17] for Zr K edge, obtained employing the random formation model.

4.9 Correction with ad-hoc path

While the accord of the data with this model is generically good and the best fit parameters of reasonable value, it is nonetheless unsatisfying due to the relatively high value of the $\Delta R_{Zr \to Ce}$ parameter, which must be investigated. As a matter of fact, the initial hypothesis relying on the cornerstone octahedral structure being the same is not necessary for the model and is very likely to be incorrect. Thus, to verify if the model is reliable also relaxing this hypothesis, a simple modification of the model was implemented using the obtained $\Delta R_{Zr \to Ce}$ parameter to introduce new, *ad-hoc* atomic coordinates for the cerium in the bimetallic cornerstone preserving its axisymmetric position in the octahedron, as shown in Figure 4.25. The fit results are shown in Table 4.6: reported uncertainties related to mean best fit values are calculated as root mean square of the values for the various datasets fitted independently.

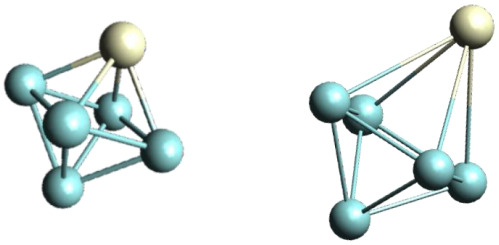

Figure 4.25: Pictorial description of the deformation of the $CeZr_5$ cornerstone. On the left, the mixed-metal cornerstone as it was first modelled, on the right, the deformed one

$S_{0,Zr}^2$	(0.85 ± 0.03)
$S_{0,Ce}^2$	(1.01 ± 0.08)
$E_{0,Zr}$	$(-0.5 \pm 0.1)\ eV$
$E_{0,Ce}$	$(1 \pm 2)\ eV$
$R_{Zr \to Zr}$	(3.515 ± 0.001) Å
$\sigma_{Zr \to Zr}^2$	(0.0041 ± 0.0002) Å^2
$R_{Zr \to Ce}$	(3.662 ± 0.004) Å
$\sigma_{Zr \to Ce}^2$	(0.0047 ± 0.0004) Å^2
$R_{Ce \to Ce}$	(3.792 ± 0.004) Å
$\sigma_{Ce \to Ce}^2$	(0.0060 ± 0.0003) Å^2
Global R factor	(0.0129 ± 0.0003)
Global reduced χ^2	(190 ± 20)
Maximum R factor	0.03 (Ce K edge-Ce 50%)
Minimum R factor	0.005 (Zr K edge-Ce 31%)
$\#_{DoG}$	52

Table 4.10: Best fit parameters for the EXAFS signals employing the deformed bimetallic cornerstone model

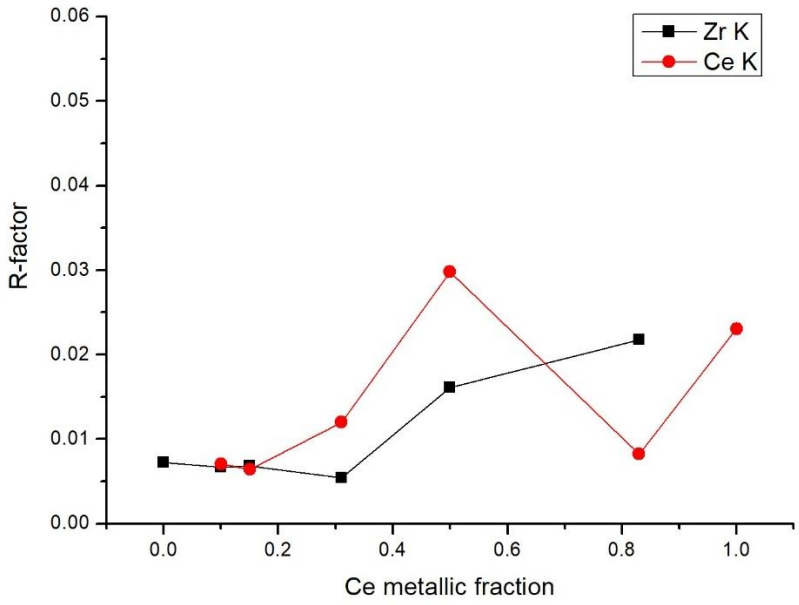

Figure 4.26: Single R-factors for the datasets presented above fitted with the preferential cornerstones' formation model with the deformed mixed-metal cornerstone

4.10 Discussion

As a final remark, it is worth summarizing the results obtained and elaborate on them a little further. A total of four different models have been employed in order to analyse the EXAFS signals obtained from the acquired data, all with the same number and type of free parameters. One assumes that the cornerstones are randomly formed, while the other three are the stoichiometric models assuming only two certain types of cornerstones per Ce:Zr concentration ratio. These latter models differ because of the k-range of EXAFS signal used for the fits and for the structural model of the mixed-metal $CeZr_5$ cornerstone, which in one model exhibits a neat deformation.

The results presented in the previous parts of this chapter are sufficient to discuss the EXAFS analysis of the MOFs spectra considered so far. First, the extremely simplified hypotheses assumed for the structural models have to be considered. The performed analysis has evidenced a weak dependence of structural parameters from the stoichiometric composition of the MOFs. Also, the analysis was not hindered by the serious limitations of the scattering paths considered for EXAFS analysis, at the cost of reducing in a controlled manner the degrees of freedom for the fits, by means of exclusion of the lower k-range after observation of single scattering amplitudes and considering only the second shell peak.

Further, the fit results have to be compared to evaluate the models that have been proposed. The fact that the random cornerstones formation model, the preferential cornerstones formation model with a reduced k-range and the preferential cornerstones formation with deformation model all have the same number and type of free parameters and degrees of freedom (in particular k and R ranges considered for the various EXAFS signals) allows to evaluate their relative quality in fitting the acquired data.

The quality of the fit using the preferential cornerstones formation model is improved over the one using the k-range from 3.7 $Å^{-1}$ by the use of a reduced k-range from 7 $Å^{-1}$: as an example, looking at Figures 4.13 and 4.22 using the reduced k-ranges 7 of 12 R-factors are lower than 0.01, while using the wider ranges there are in fact some high R-factors for the single signals. While the precise reason why this happens is not straightforward to establish, some plausible causes can be traced to the differences between the two beamlines and the overall worse quality of the data acquired at the edge of a metal with lower

concentration in the MOF sample. Also, generically speaking it seems that the datasets corresponding to samples with higher cerium concentrations are fitted worse.

However, the structural results are compatible with the ones obtained with a wider k-range, especially the $\Delta R_{Zr \to Ce}$ parameter, which is the most important deformation of the assumed octahedral structural model of the cornerstone. This fact reassures about the correctness of the choice of k-range cut-off: it does not distort the structural description of the cornerstones.

After elucidating this, it must be considered that the randomized structural model fits the data worse than the one with preferential cornerstones formation as can be seen for the higher global reduced χ^2 and global R factor. Also, looking at Figure 4.23, 3 out of 12 spectra have R factor higher than 0.08 and 5 out of 12 have R factor higher than 0.03: thus, the quality of the fits may be considered very low and we may reject this hypothesis in favour of a preferential formation of pure and $CeZr_5$ cornerstones.

As a final remark, the two-cornerstones model with a deformation of the mixed-metal $CeZr_5$ cornerstones may be considered equivalent to the main one with regards to its quality. Further, the results of the fits show that the structural results for this model are compatible with the ones obtained from the main model, also considering the $R_{Zr \to Ce}$ parameter, allowing to conclude that the fitting procedure is genuine.

Bibliography: Chapter 4

Ankudinov, A., & al., e. (1998). Real Space Multiple Scattering Calculation and Interpretation of X-Ray Absorption Near Edge Structure. *Phys. Rev. B58*, 7565.

Bunker, G. ((2010)). *Introduction to XAFS_ A Practical Guide to X-ray Absorption Fine Structure Spectroscopy.* Cambridge University Press .

Calvin, S. (2013). *XAFS for everyone.* CRC Press Taylor & Francis Group.

Fornasini, P. (2001). Study of lattice dynamics via extended x-ray absorption fine structure. *J. Phys.: Condens. Matter 13*, 7859-7872.

Lomachenko, K., & al., e. (2018). Exact stoichiometry of CeZr cornerstones in mixed-metal UiO-66 MOFs revealed by EXAFS spectroscopy. *J. Am. Chem. Soc.*

Ravel, B. &. ((2005)). ATHENA, ARTEMIS, HEPHAESTUS: data analysis for X-ray absorption spectroscopy using IFEFFIT. *Journal of Synchrotron Radiation 12*, 537–541.

Smolders, S., & al., e. (2018). Unravelling the Redox-catalytic Behavior of Ce 4+ Metal–Organic Frameworks by X-ray Absorption Spectroscopy. *ChemPhysChem, 19*, 373-378.

Conclusions

In this thesis the bimetallic MOF Zr/Ce-UiO-66 has been investigated by means of Extended Absorption X-ray Fine Structure (EXAFS) spectroscopy. In order to perform the analysis, the data were acquired at the ESRF synchrotron in Grenoble, at the beamlines BM23 and BM31 at Ce and Zr K edge. Data were also acquired at the Ce L_3-edge, but only for the identification of the chemical state of the cerium present, which resulted to be mostly in the Ce(IV) form, in agreement with the presence of UiO-66 octahedral cornerstones.

The methods of analysis and the models used to investigate the stoichiometry of its cornerstones have been presented. Compatibility of the data obtained at different beamlines had to be established and quantified through the parametrization of the fitting curves. Regarding this point, EXAFS analysis of well-known samples of cerium and zirconium oxides have been performed on data taken at both the beamlines. The results have been used to put simple constraints on analogous parameters for spectra acquired at different beamlines.

If the stoichiometry of the cornerstones is the main property enquired, the EXAFS fits may be performed only on the second shell peak for each of the twelve spectra fitted together (six at Ce K edge and six at Zr K edge), using only the single scattering paths involving metal atoms. This extremely simplified assumption may yield a significative fit if the k-range used is accurately chosen, after an inspection of the relative magnitude of the scattering amplitudes for paths involving metal atoms and those involving oxygen atoms. The structural results from the fits performed using different k-ranges have been found to be compatible.

Particular interest has been placed in the metallic composition of the octahedral cornerstones present in the MOF. This is due to the fact that an accurate knowledge of the cornerstones' stoichiometry is essential to the understanding of the macroscopic properties of these MOFs (e.g. decomposition temperature trend with Ce metallic fraction (Lammert & al., Tuning the stability of bimetallic Ce(IV)/Zr(IV)-based MOFs with UiO-66 and MOF-808 structures, 2015)). Also, this is a step forward in the assessment of their catalytical properties, which are plausibly dependent from the exact configuration of the active sites (i.e. cerium atoms) in the cornerstones.

Two stoichiometric models have been investigated: one assuming only two types of cornerstones per Ce metallic fraction, distinguishing the $[Ce] < 1/6$ and $[Ce] > 1/6$ regimes, the other assuming a randomized formation of the cornerstones with regards to the metal atoms. In the first, for $[Ce] < 1/6$ only cornerstones of $CeZr_5$ and Zr_6 types are assumed to be present, while for $[Ce] > 1/6$ only $CeZr_5$ and Ce_6 types. In the second one, each metallic site of the cornerstones is occupied by a certain type of metal atom with a probability given by the concentration of the metal in the sample.

Since the degrees of freedom in the two models are the same, with only the coordination numbers differing neatly, it has been possible to compare the relative fit results. We can therefore deduce from this analysis that the random formation of cornerstones is to be rejected in favour of a model involving preferential formation of some types of cornerstones. The deviation of mixed-metal $CeZr_5$ cornerstones from octahedral shape has been briefly investigated to explain large values of the $\Delta R_{Zr \to Ce}$ parameter as a deformation of the cornerstones themselves.

As a final point, it is worth to briefly link this work to a previous work on the subject reported in (Lomachenko & al., 2018): the main conclusion about cornerstones stoichiometry is confirmed and in this work a comparison with a null hypothesis (the random cornerstones formation model) is also made, thus reinforcing the two-cornerstones model itself.